Supplementary Materials for

N-bridged Co-N-Ni: new bimetallic sites for promoting electrochemical CO_2 reduction

Jiajing Pei,‡ [a] Tao Wang,‡ [b] Rui Sui,[a] Xuejiang Zhang,[a] Danni Zhou,[c] Fengjuan Qin,[c] Xu Zhao,[d] Qinghua Liu,[d] Wensheng Yan,[d] Juncai Dong,[e] Lirong Zheng,[e] Ang Li,[f] Junjie Mao,*[g] Wei Zhu,[a] Wenxing Chen,*[c] and Zhongbin Zhuang*[a]

[a] State Key Lab of Organic-Inorganic Composites, College of Chemical Engineering, Beijing University of Chemical Technology, Beijing 100029, China

[b] Center of Artificial Photosynthesis for Solar Fuels, School of Science, Westlake University, Hangzhou 310024, China

[c] Energy & Catalysis Center, School of Materials Science and Engineering, Beijing Institute of Technology, Beijing 100081, China

[d] National Synchrotron Radiation Laboratory, University of Science and Technology of China, Hefei 230029, China

[e] Beijing Synchrotron Radiation Facility, Institute of High Energy Physics, Chinese Academy of Science, Beijing 100049, China

[f] Institute of Microstructure and Property of Advanced Materials, Beijing University of Technology, Beijing 100124, China

[g] College of Chemistry and Materials Science, Anhui Normal University, Wuhu, 241002, China

‡ These authors contributed equally to this work.

* Corresponding author. E-mail: maochem@ahnu.edu.cn, wxchen@bit.edu.cn, zhuangzb@mail.buct.edu.cn.

Table of contents

Section 1: Experiment details

Reagents. Cobalt (II) phthalocyanine (CoPc), nickel phthalocyanine (NiPc), α-cellulose, melamine, Potassium bicarbonate, Nafion D-521 dispersion (5% w/w in water and 1-propanol), were purchased from Alfa Aesar. Methanol, ethanol and KOH (analytical grade) were obtained from Sinopharm Chemical. Hydrochloric acid (~37%) was obtained from Beijing Chemical Reagents. Nafion 211 membrane was purchased from Dupont. 18.2 MΩ cm ultrapure water was purified by milli-Q instrument. High purity Helium gas (99.9999%) and carbon dioxide (99.999%) were purchased at Haipu Gas Company. All the chemicals were analytical grade and used without further purification.

Synthesis of porous carbon nanosheets (PCNSs).

The PCNSs was prepared by pyrolysis method reported in the literature.[1] In a typical synthesis, 5 g of α-cellulose and potassium bicarbonate with a mass ratio of 1:2 were evenly ground. Then put the homogeneous mixture in a porcelain boat and heated at 800 ℃ for 90 min under N_2 atmosphere in a tube furnace with a heating rate of 10 ℃/min. After cooling down to room temperature, the samples were dispersed in 2 M HCl solution and then stirred for 12 h. The PCNSs powders were obtained after filtrating with deionized water and drying at 60 °C in vacuum oven overnight.

Synthesis of Co-N-Ni/NPCNSs.

In brief, PCNSs (200 mg) and melamine (500 mg) were dispersed in 120 ml of water and ethanol mixture (v/v =1:1) and sonicated for 1h. Then the moderate ethanol solution containing CoPc and NiPc (25 mg/mL, 140 μL) was dropwise added into the above solution under stirring. Subsequently, the mixture solution was stirred for 24 h and washed thoroughly with ethanol for several times. Finally, the samples were dried at 60 ℃ for overnight. The as-prepared sample was annealed at 1000 ℃ under the N_2 atmosphere for 1 h with a ramping rate of 5 ℃/min. The preparation of Co-N/NPCNSs and Ni-N/NPCNSs is similar as the process for Co-N-Ni/NPCNSs except for adding the relative precursor separately, denoted as Co-N/NPCNSs and Ni-N/NPCNSs.

Characterizations. The morphology of the samples characterized by transmission electron microscope (TEM) was operated by a Hitachi-7700 working at 100 kV. The HAADF-STEM images were obtained by FEI Tecnai G2 F20 S-Twin HRTEM which worked at 200 kV. The atomic resolution high-angle annular dark-field scanning TEM (HAADF-STEM) images of all catalysts were collected on a high-resolution transmission electron microscopy (JEM-ARM200F working at 300 kV), equipped with a probe spherical aberration corrector. The metal content of single atom catalysts was gauged by Inductively coupled plasma mass spectrometry (ICP-MS), which was carried out on Thermo Fisher X II. Powder X-ray diffraction pattern (PXRD) was used a Rigaku D/max 2500Pc X-ray powder diffractometer with monochromatized Mo Kα radiation (λ =0.7107 Å). The N_2 adsorption/desorption curve was characterized by Brunauer-Emmett-Teller (BET) method using a Micromeritics ASAP 2020 surface area analyzer.

Photoemission spectroscopy experiments were carried out at the Catalysis and Surface Science End station at the BL11U beamline in the National Synchrotron Radiation Laboratory (NSRL) in Hefei, China. This beamline is connected to an undulator and equipped with two gratings that offer soft X-rays from 20 to 600 eV, and equipped with a VG Scienta R4000 analyzer, a monochromatic Al K*a* X-ray source. Co 2p and Ni 2p spectra were collected by the monochromatic Al K*a* X-ray source, hν=1486.6 eV. N 1s spectra were collected by synchrotron light, hν=500 eV. For the core-level spectra, the binding energies were calibrated using the C 1s feature located at 285.0 eV as the reference.

Electrochemical measurements for CO_2RR. Electrochemical experiments were measured on CHI 660E electrochemical workstation (Shanghai Chenhua, China) with a H-type electrochemical cell in 0.1M $KHCO_3$ (pH = 8) electrolyte. The HCP120 carbon paper, Pt wire and Ag/AgCl (saturated KCl) was used as working electrode, counter electrode and reference electrode respectively. Nafion 211 membrane was inserted between the cathodic chamber and anodic chamber of H-type cell. Before all measurements, the $KHCO_3$ aqueous solution was purified by bubbling Ar for 30 min and then switched to CO_2 until saturation. To prepared the working electrolyte, 5 mg of

as-prepared Co-N-Ni/NPCNSs catalyst or the reference SSCs and 10 μL of 5% Nafion solution were added into 240 μL of water and 750 μL of isopropyl alcohol, and then sonicated for 4 h. The total catalyst loading on HCP120 carbon paper is 1mg/cm^2. The Co-N&Ni-N/NPCNSs physical mixture catalyst was prepared by physical mixing and grinding evenly of Co and Ni single-site catalysts, and their mixing ratio was 1:1. The LSV curves were conducted at scan rate of 10 mV/s with always bubbling CO_2 at flow rate of 15 sccm via a flow meter. All the potential was reported versus the reversible hydrogen electrode (RHE) and corrected by iR drop compensation. The chronoamperometry tests were conducted at each potential for 37.75 min. The gas products of CO_2RR were checked via the Shimazu 2010 plus gas chromatography (GC), which was equipped with BID detector and ShinCarbon ST 100/120 packed column. High purity helium (99.9999%) was used as the carrier gas for the chromatography. The Faraday efficiency of gas products was calculated by the equation:

$$FE\ \% = \frac{\left[V_{H_2}(\mu l) + V_{CO}(\mu l)\right] \times n \times F(C/mol) \times 10^{-6}(L/\mu l)}{I_{total}(C/s) \times t(s) \times 22.4(L/mol)} \times 100\%$$

$V_{H_2}(\mu l) + V_{CO}(\mu l)$ = volume of H_2 and CO in the gas product from the H-type cell (GC data).

$I_{total}(C/s)$ = H-type cell steady-state current at each potential.

n = 2, the number of electron transferred for product formation, which is 2 for both CO and H_2 production.

F = 96485 C mol^{-1}, Faradaic constant.

t = 4 s, the time of gas products to enter the GC.

TOF for CO production was calculated as follow equation:

$$TOF = \frac{I_{product}/nF}{m_{cat} \times \omega / M_{metal}} \times 3600$$

TOF = turnover frequency, h^{-1}.

$I_{product}$ = partial current for certain product, A.

n = 2, the number of electrons transferred for CO production.

F = 96485 C mol^{-1}, Faradaic constant.

m_{cat} = the mass of catalyst on the carbon paper, g.

ω = metal loading in the catalyst.

M_{metal} = atomic mass of Ni (58.69 g mol^{-1}) for Ni-N/NPCNSs, atomic mass of Co (58.93 g mol^{-1}) for Co-N/NPCNSs, and atomic mass of 58.81 g mol^{-1} for Co-N-Ni/NPCNSs (based on the ratio of Ni and Co).

Ex-situ XAFS and Soft-XAS measurements. The XAFS spectra data (Co K-edge, Ni K-edge) were tested at 1W1B station in Beijing Synchrotron Radiation Facility (BSRF, operated at 2.5 GeV with a maximum current of 250 mA). The XAFS data of the samples were collected at room temperature in fluorescence excitation mode using a Lytle detector. All the samples were added with graphite and ground uniformly, and then pressed into a10 mm plate with a thickness of 1 mm. The XANES spectra of C K-edge and N K-edge were measured at beamline BL12B of National Synchrotron Radiation Laboratory (NSRL). The moderate samples were overlaid onto conductive tape for X-ray spectroscopy.

XAFS data processing.

The received EXAFS data were processed according to the standard procedures using the Athena and Artemis implemented in the IFEFFIT software packages. The fitting detail is depicted in the following:

The EXAFS spectra were obtained by subtracting the post-edge background from the overall absorption and then normalizing relative to the edge-jump step. Subsequently, the $\chi(k)$ data of were Fourier transformed to real (R) space using a hanning windows (dk=1.0 $Å^{-1}$) to separate the EXAFS contributions from different coordination shells. To obtain the quantitative structural parameters around central atoms, least-squares curve parameter fitting was performed using the ARTEMIS module of IFEFFIT software packages.[2]

The following EXAFS equation was used:

$$\chi(k) = \sum_j \frac{N_j S_o^2 F_j(k)}{k R_j^2} \exp[-2 k^2 \sigma_j^2] \exp[\frac{-2 R_j}{\lambda(k)}] \sin[2k R_j + \phi_j(k)]$$

S_0^2 is the amplitude reduction factor, $F_j(k)$ is the effective curved-wave backscattering amplitude, N_j is the number of neighbors in the j^{th} atomic shell, R_j is the distance between the X-ray absorbing central atom and the atoms in the j^{th} atomic shell (backscatterer), λ is the mean free path in Å, $\phi_j(k)$ is the phase shift (including the phase shift for each shell and the total central atom phase shift), σ_j is the Debye-Waller parameter of the j^{th} atomic shell (variation of distances around the average R_j). The functions $F_j(k)$, λ and $\phi_j(k)$ were calculated with the ab initio code FEFF8.2. The additional details for EXAFS simulations are given below.

The coordination numbers of model samples (Co and Ni foil) were fixed as the nominal values. The obtained S_0^2 was fixed in the subsequent fitting of Co and Ni single atom samples. While the internal atomic distances R, Debye-Waller factor σ^2, and the edge-energy shift ΔE_0 were allowed to run freely.

In-situ SR-FTIR measurements. In-situ SRFTIR spectroscopy measurements were made at the infrared beamline BL01B of National Synchrotron Radiation Laboratory (NSRL) through a homemade top plate cell reflection infrared set-up with a ZnSe crystal as the infrared transmission window (cutoff energy of ~625 cm−1). The end station was equipped with a FTIR spectrometer (Bruker 66 v/s) with a KBr beam-splitter and various detectors (here a liquid nitrogen cooled mercury cadmium telluride detector was used) coupled with an infrared microscope (Bruker Hyperion 3000) with a ×16 objective, and can provide infrared spectroscopy measurement with a broad range of 15-4,000 cm^{-1} as well as a high spectral resolution of 0.25 cm^{-1}. The catalyst electrode is tightly pressed against the ZnSe crystal window with a micrometre-scale gap to reduce the loss of infrared light. To ensure the quality of the obtained FTIR spectra, the apparatus was used in a reflection mode with a vertical incidence of infrared light. Each infrared absorption spectrum was acquired by averaging 256 scans at a resolution of 2 cm^{-1}. To guarantee the sustainability of the CO_2RR reactions, CO_2 saturation was appropriated via peristaltic pumps with a flow rate of 50 μl h^{-1} during in situ infrared reflection measurements. All infrared spectral acquisitions were carried

out after a constant potential was applied to the catalysts electrode for 20 min. The background spectrum of the catalyst electrode was acquired at an open-circuit voltage before each systemic CO_2RR measurement, and the measured potential ranges of the CO_2RR were -0.1~ -0.8 V vs RHE.

In-situ Electrochemical XAS Measurements. An orgonic glass electrochemical cell is employed for in situ spectroscopic experiments. The working compartment has flat walls with a single circular hole of 1.5 cm in diameter. The Co-N-Ni/NPCNSs coated carbon cloth is in contact with a slip of copper with the Co-N-Ni/NPCNSs layer facing inward. Then 0.1 M $KHCO_3$ solution is poured into the compartment. The solutions are not stirred during the experiment. The cell is connected to an electrochemical workstation by making electrical contact to the copper tape slip that protruded from the side of the working compartment. An orgonic glass cap fitted with a reference electrode (SCE) is used to cover the working compartment and to ensure a fixed distance between working and reference electrodes for all experiments. The X-ray absorption spectra are recorded at different positions on the electrode to check the materials for homogeneity. The same electrodes are used to measure the Co and Ni K-edge (BL1W1B) spectra. Spectra were recorded on the dry Co-N-Ni/NPCNSs films at first and then in 0.1 M $KHCO_3$ solution at different potentials.

Computational details. All the DFT calculations were carried out with the Vienna Ab Initio Simulation Package (VASP). [3,4] The electron ion interaction was described with the projector augmented wave (PAW) method.[5,6] The revised Perdew-Burke-Ernzerhof (RPBE) exchange-correlation functional was applied to solve the electron exchange and correlation energy within the generalized gradient approximation.[7] An energy cut-off of 400 eV and a second-order Methfessel-Paxton electron smearing with σ = 0.2 eV were used. The convergences for energy and force are 10^{-5} eV and 0.02 eV/Å, respectively. A vacuum layer of 15 Å was set between the periodically repeating slabs to avoid obvious interactions. Spin polarization was considered throughout all the calculations. The CO_2 reduction to CO mechanism contains proton-electron transfers: (1) $CO_2(g) + * + e^- \leftrightarrow *CO_2^-$, (2) $*CO_2^- + H^+ \leftrightarrow *COOH$; (3) $*COOH + e^- + H^+ \leftrightarrow *CO + H_2O$; (4) $*CO \leftrightarrow CO(g) + *$, where asterisk * denotes the active site. The free

energy of the reaction was calculated with computational hydrogen electrode (CHE) model as developed by Norskov group,[8,9] which provides an elegant approach of avoiding the explicit treatment of solvated protons.

Section 2: Supplementary Figures and Tables

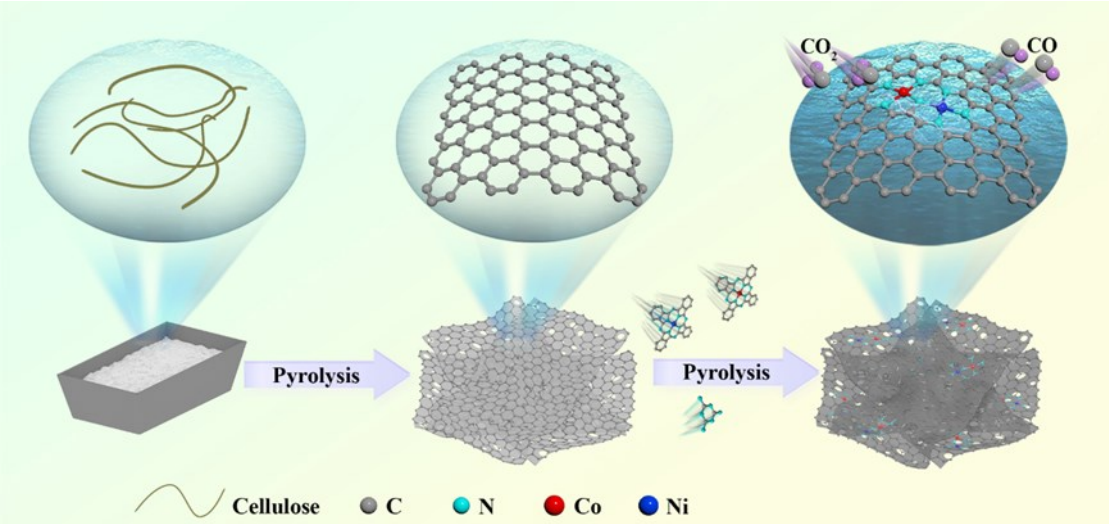

Fig. S1. Schematic illustration of synthetic procedure of the Co-N-Ni/NPCNSs.

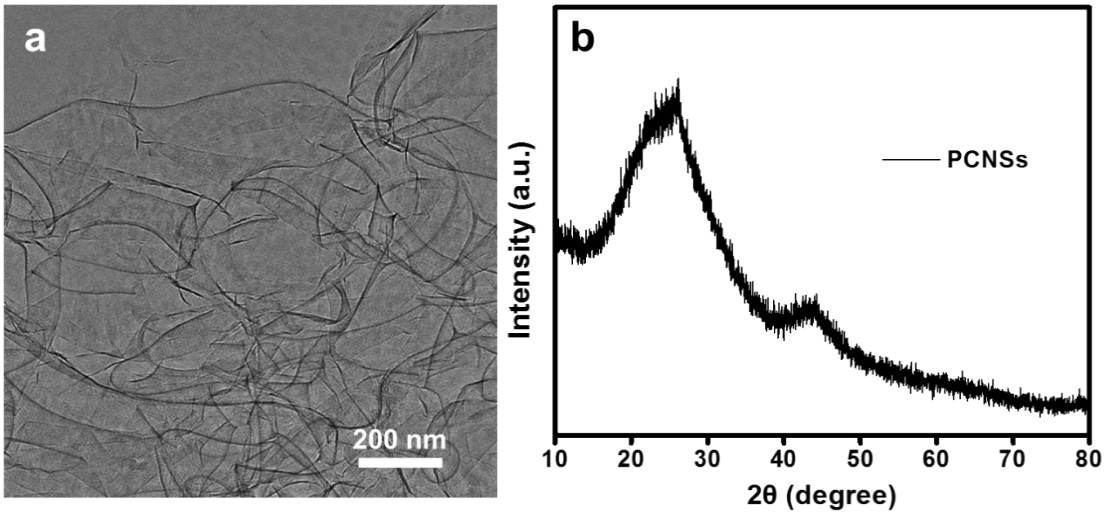

Fig. S2. (a) TEM image and (b) XRD pattern of the PCNSs.

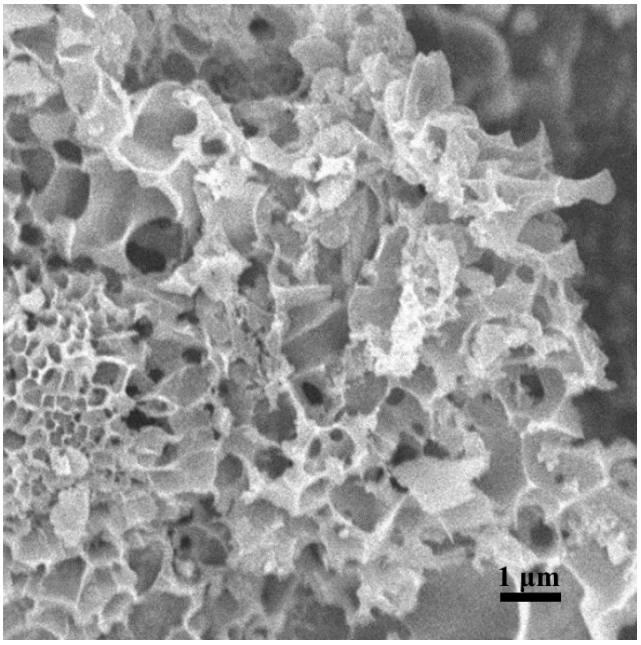

Fig. S3. SEM image of Co-N-Ni/NPCNSs.

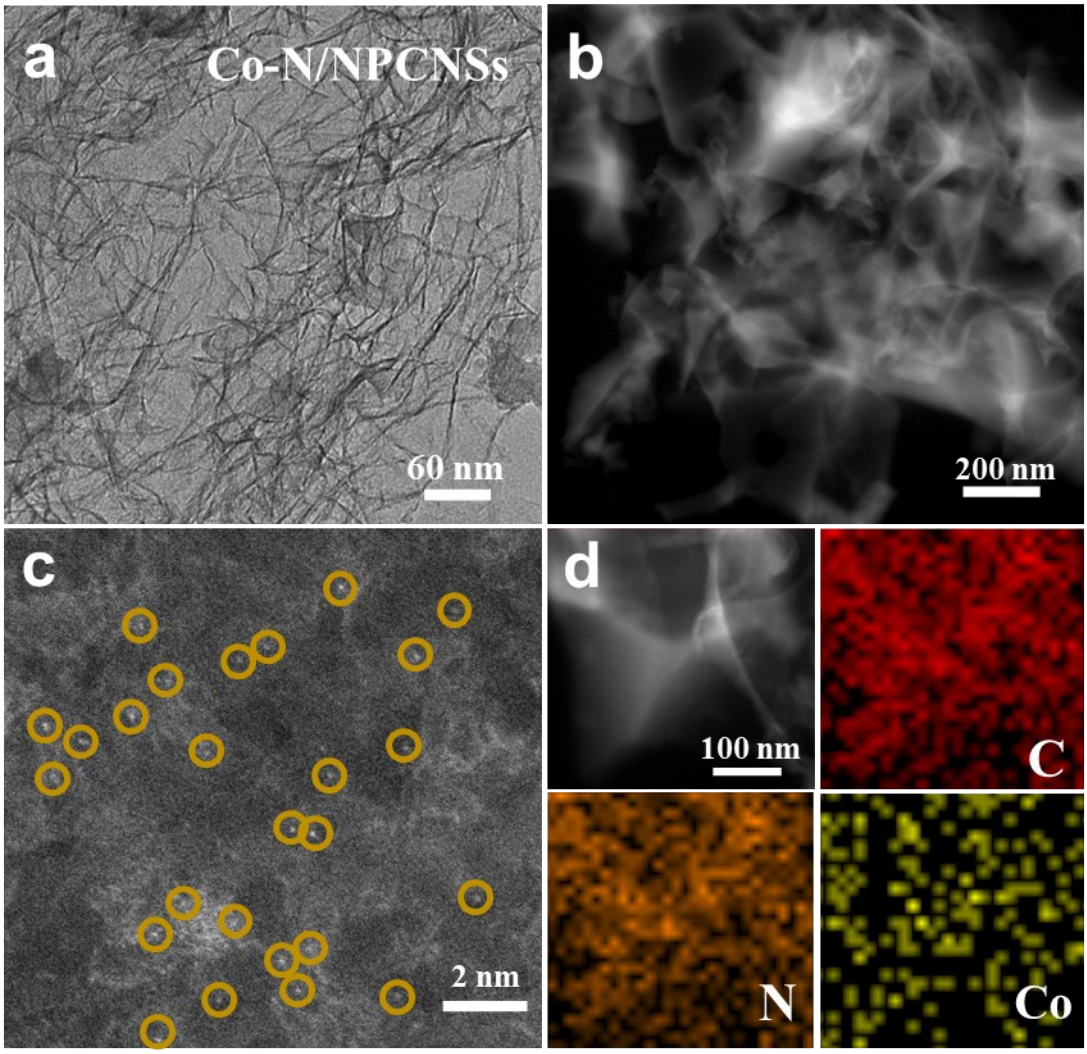

Fig. S4. (a) TEM and (b) HAADF-STEM images of Co-N/NPCNSs. (c) The aberration-corrected HAADF-STEM image of Co-N/NPCNSs. Each bright spot is surrounded by an orange circle representing a Co single-atom, and demonstrating the atomic dispersion of the Co species. (d) EDS mapping images of C (red), N (orange) and Co (yellow) for Co-N/NPCNSs, revealing the homogeneous distribution of Co and N on the carbon substrate.

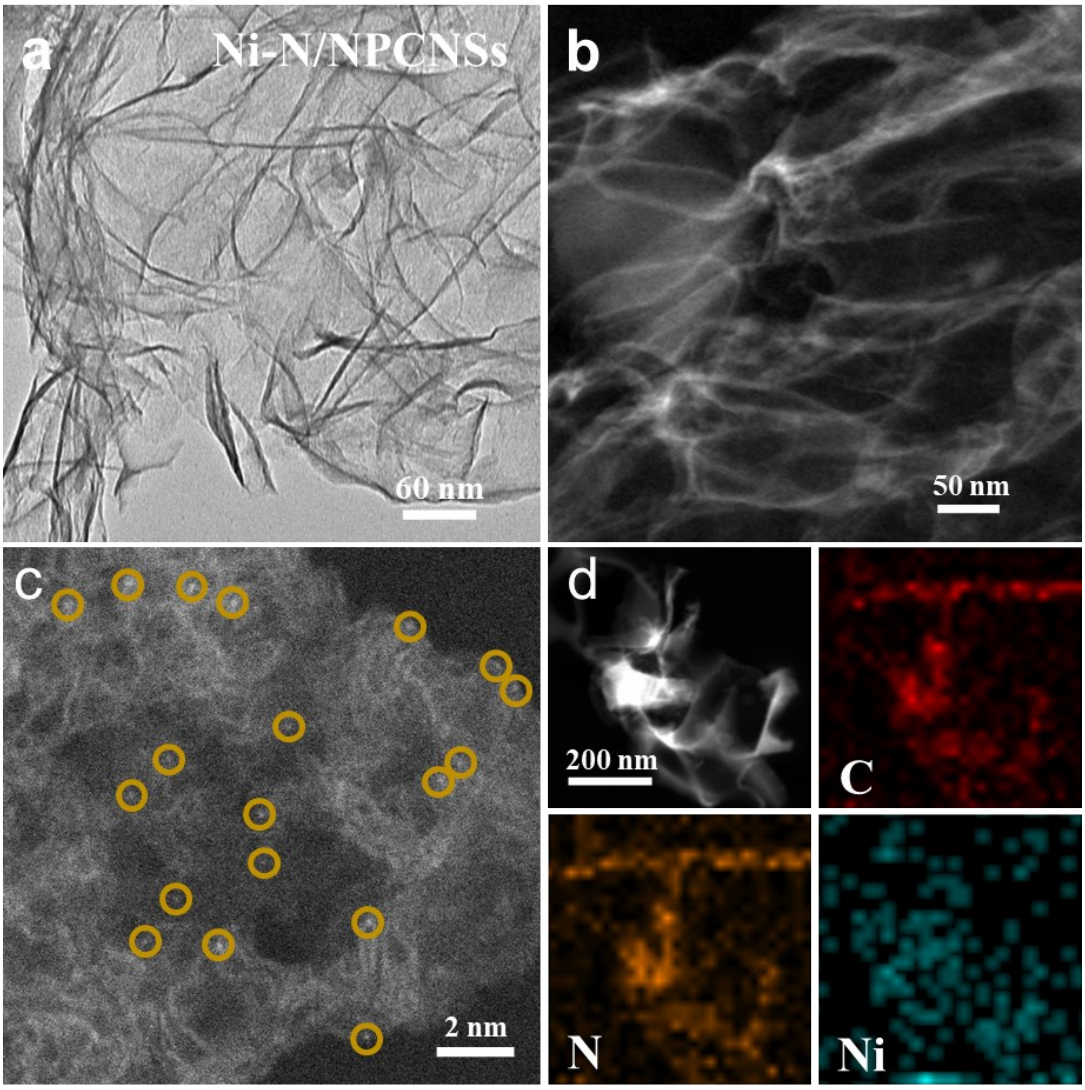

Fig. S5. (a) TEM and (b) HAADF-STEM images of Ni-N/NPCNSs. (c) The aberration-corrected HAADF-STEM image of Ni-N/NPCNSs, each bright spot in the orange circle represents a single Ni atom, suggesting the atomic dispersion of the Ni species. (d) EDS mapping images of C (red), N (orange) and Ni (blue-green) for Ni-N/NPCNSs, denoting the homogeneous distribution of Ni and N on the whole carbon matrix.

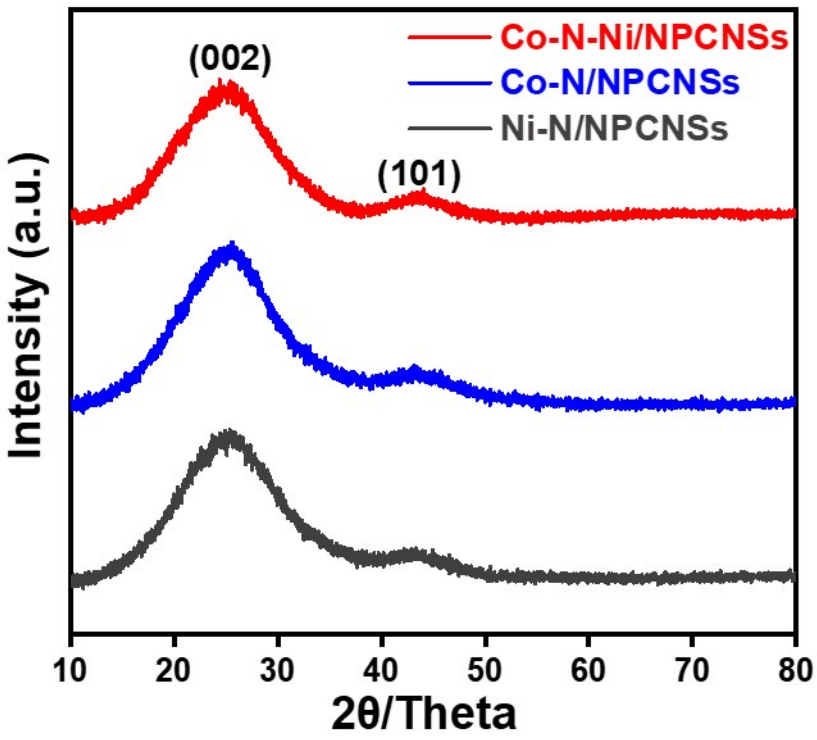

Fig. S6. XRD patterns of Co-N-Ni/NPCNSs, Co-N/NPCNSs and Ni-N/NPCNSs. From Fig. S6, we only observe two characteristic peaks of C, and no signals ascribed to metallic/oxidic Co or Ni are emerged. The wide peak with strong intensity at 25 degree is assigned to (002) plane of C, and another weak peak at 43 degree is distributed to (101) plane of C. Therefore, we can eliminate the interference of Cu Kα radiation source, and claim that the Co or Ni species are atomically dispersed on the N-doped porous carbon nanosheets.

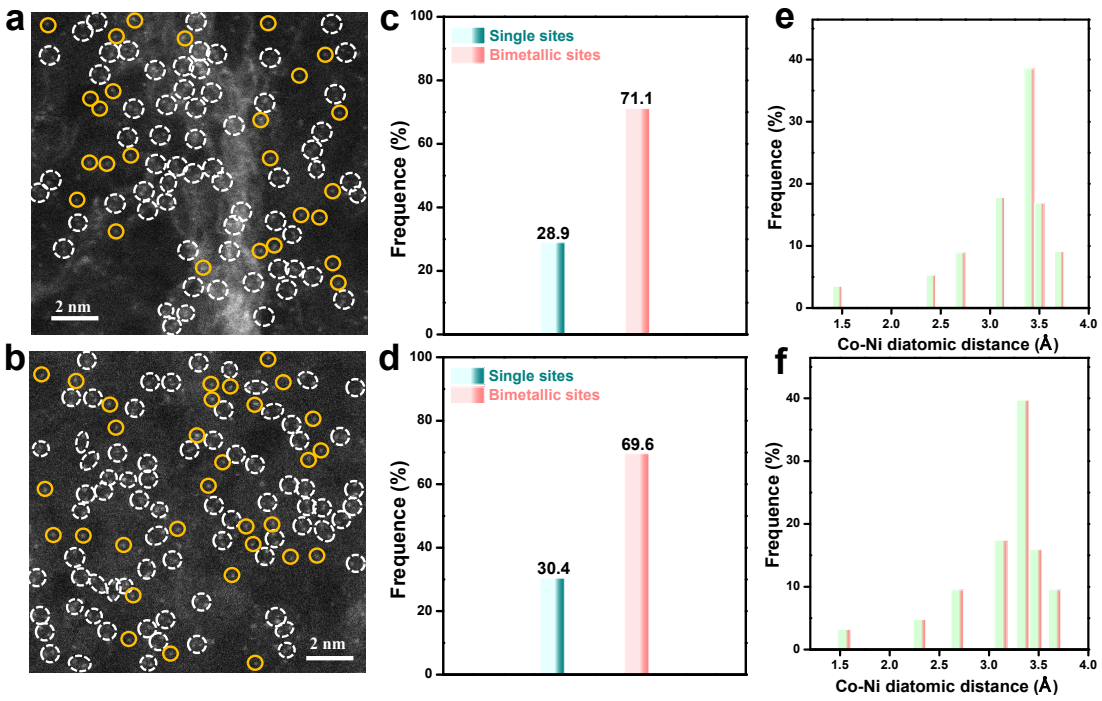

Fig. S7. (a, b) The AC-STEM image of Co-N-Ni/NPCNSs catalyst. The bimetallic sites and single sites were marked by dotted white circles and orange solid circles, respectively. (c, d) Statistical the density of Co-N-Ni bimetallic sites and single sites in AC-STEM images (a, b). (e, f) Statistical Co-Ni diatomic distance in AC-STEM images (a, b).

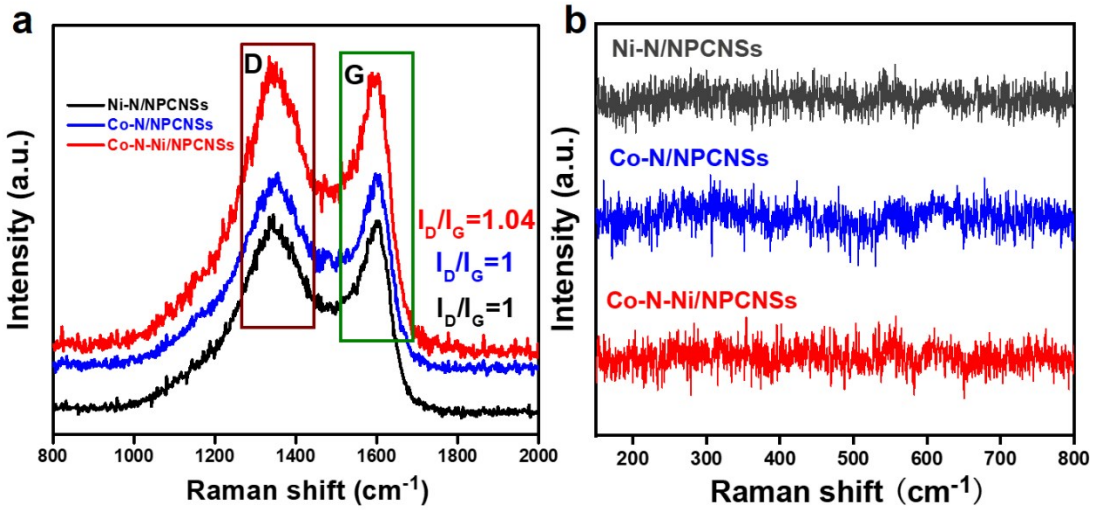

Fig. S8. (a) The Raman spectra of the Co-N-Ni/NPCNSs, Co-N/NPCNSs and Ni-N/NPCNSs. As shown in the Raman spectra, two characteristic peaks of carbon at 1347 cm^{-1} (D band, disordered/defective carbon) and 1597 cm^{-1} (G band, graphitic carbon) were discovered. The Co-N-Ni/NPCNSs catalyst possesses the optimal I_D/I_G value (1.04). The high ratio of I_D is beneficial for anchoring metal atoms on the carbon matrix. (b) The Raman spectra of Ni-N/NPCNSs, Co-N/NPCNSs, and Co-N-Ni/NPCNSs measured at a wavenumber window between 150 and 800 cm^{-1}. No vibration modes assigned to CoO_x or NiO_x were found. It further suggested that no metal oxides were formed in the three samples.

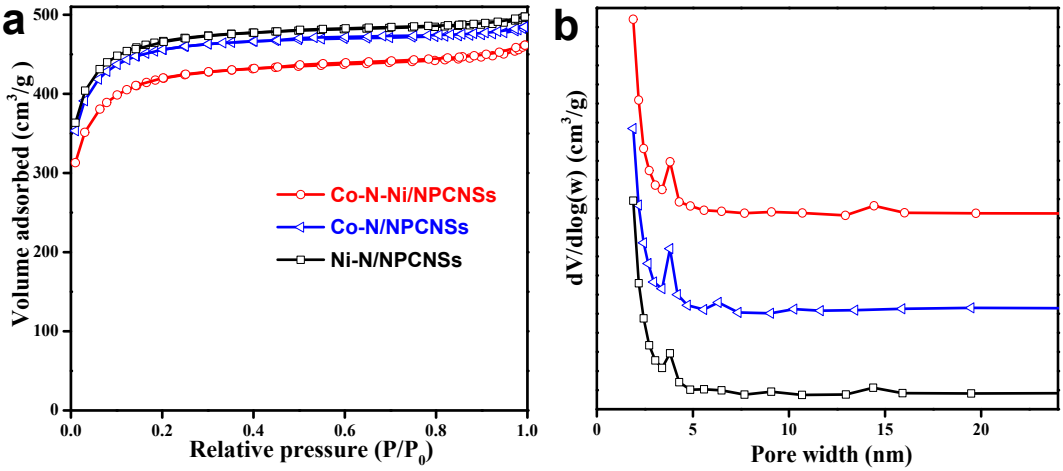

Fig. S9. N_2 adsorption-desorption isotherms (a) and pore size distribution (b) of Co-N-Ni/NPCNSs, Co-N/NPCNSs and Ni-N/NPCNSs. The specific surface area of Co-N-Ni/NPCNSs, Co-N/NPCNSs and Ni-N/NPCNSs is 1515, 1575 and 1585 m^2 g^{-1}, respectively. The pore size distribution of all catalysts is dominated by micropores.

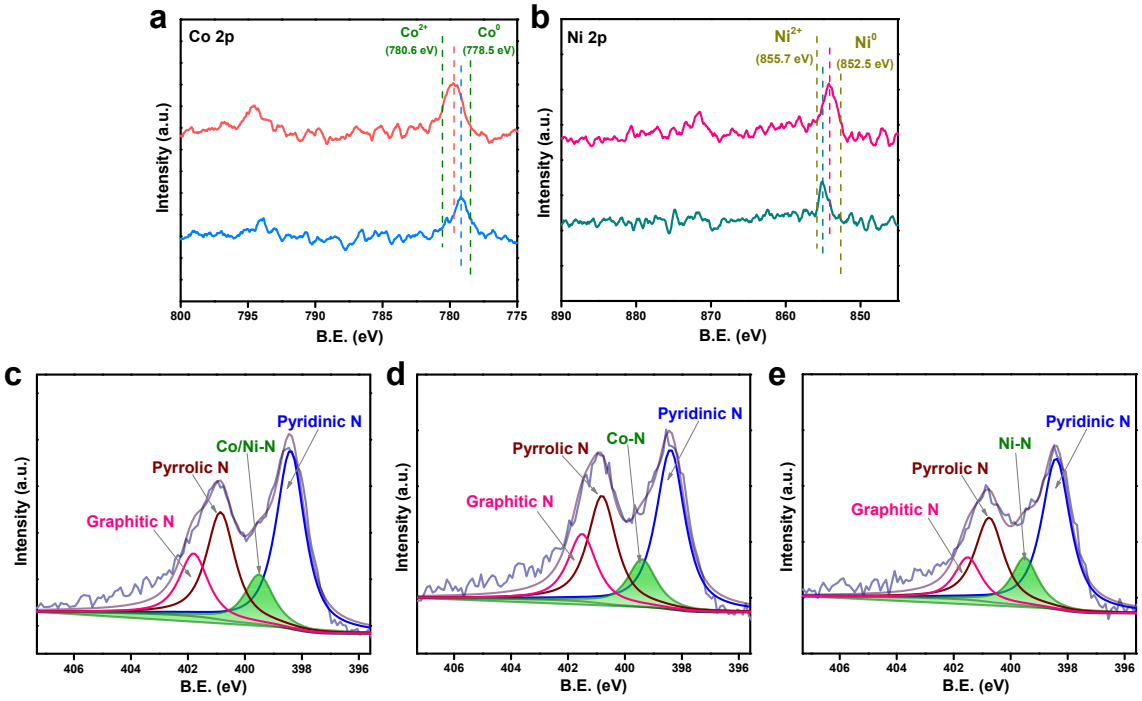

Fig. S10. The high-resolution XPS spectra of Co-N-Ni/NPCNSs, Co-N/NPCNSs and Ni-N/NPCNSs catalysts. (a) Co 2p. (b) Ni 2p. N 1s spectrum of Co-N-Ni/NPCNSs (c), Co-N/NPCNSs (d), and Ni-N/NPCNSs (e).

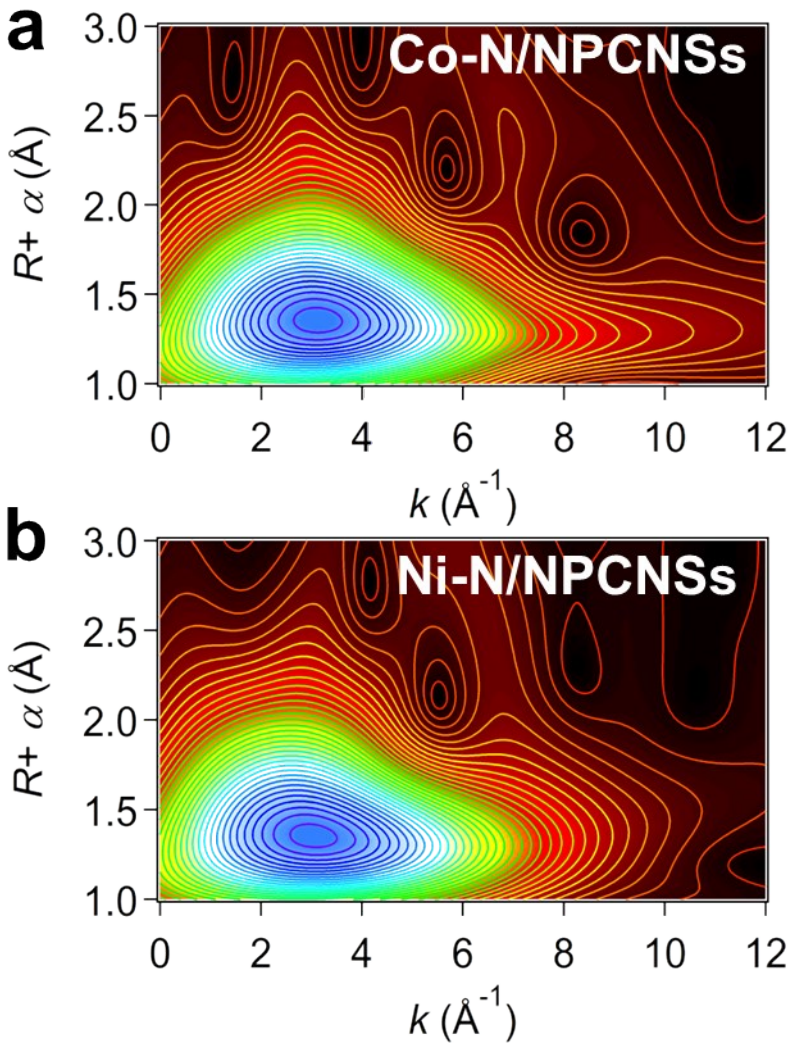

Fig. S11. The WT plots of the corresponding Co-N/NPCNSs (a) and Ni-N/NPCNSs (b) catalysts.

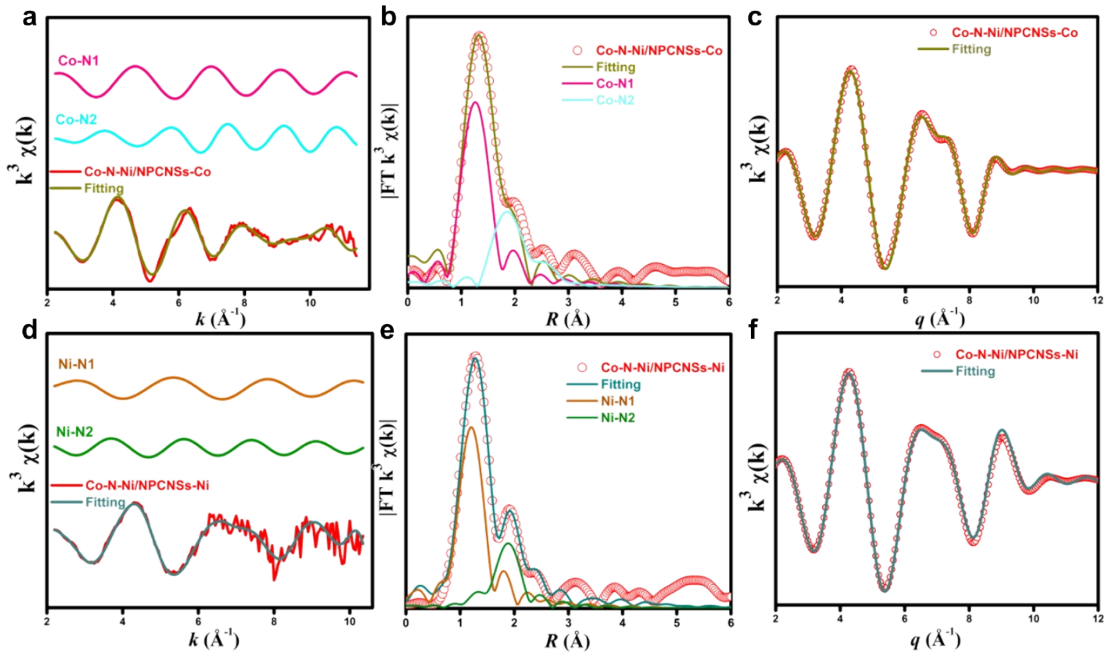

Fig. S12. FT-EXAFS fitting curve on the basis of Co-N-Ni/NPCNSs. (a) The *k*-space EXAFS curve at Co K-edge. (b) The *r*-space EXAFS curve at Co K-edge. (c) The *q*-space EXAFS curve at Co K-edge. (d) The *k*-space EXAFS curve at Ni K-edge. (e) The *R*-space EXAFS curve at Ni K-edge. (f) The *q*-space EXAFS curve at Ni K-edge.

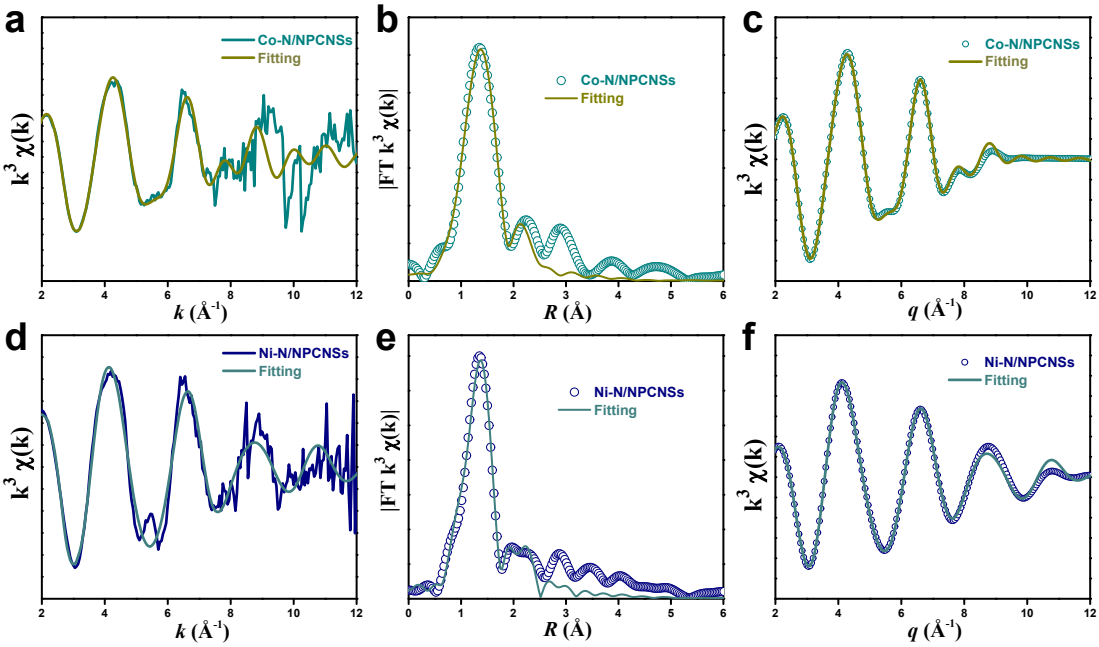

Fig. S13. FT-EXAFS fitting curve on the basis of Co-N/NPCNSs and Ni-N/NPCNSs. (a)The *k*-space EXAFS curve at Co K-edge of Co-N/NPCNSs. (b) The *R*-space EXAFS curve at Co K-edge of Co-N/NPCNSs. (c) The *q*-space EXAFS curve at Co K-edge of Co-N/NPCNSs. (d) The *k*-space EXAFS curve at Ni K-edge of Ni-N/NPCNSs. (e) The *R*-space EXAFS curve at Ni K-edge of Ni-N/NPCNSs. (f) The *q*-space EXAFS curve at Ni K-edge of Ni-N/NPCNSs.

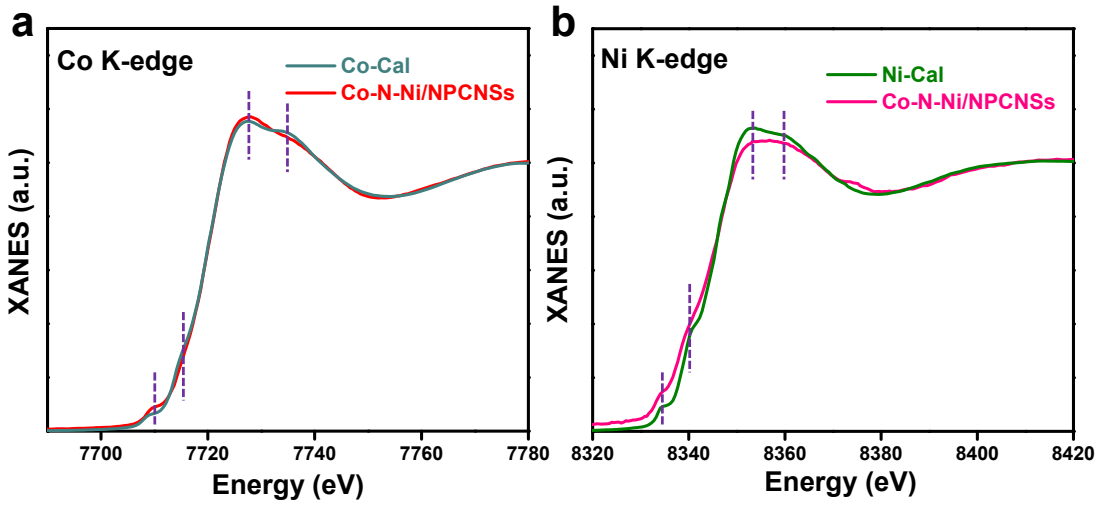

Fig. S14. The simulated XANES spectrum of (a) Co K-edge and (b) Ni K-edge based on the N-bridged Co-N-Ni model, compared with the experimental spectrum of Co-N-Ni/NPCNSs. The Co K-edge and Ni K-edge theoretical XANES simulations were carried out with the FDMNES code in the framework of real-space full multiple-scattering (FMS) scheme using Muffin-tin approximation for the potential. The energy dependent exchange-correlation potential was calculated in the real Hedin-Lundqvist scheme, and then the spectra convoluted using a Lorentzian function with an energy-dependent width to account for the broadening due both to the core-hole width and to the final state width.

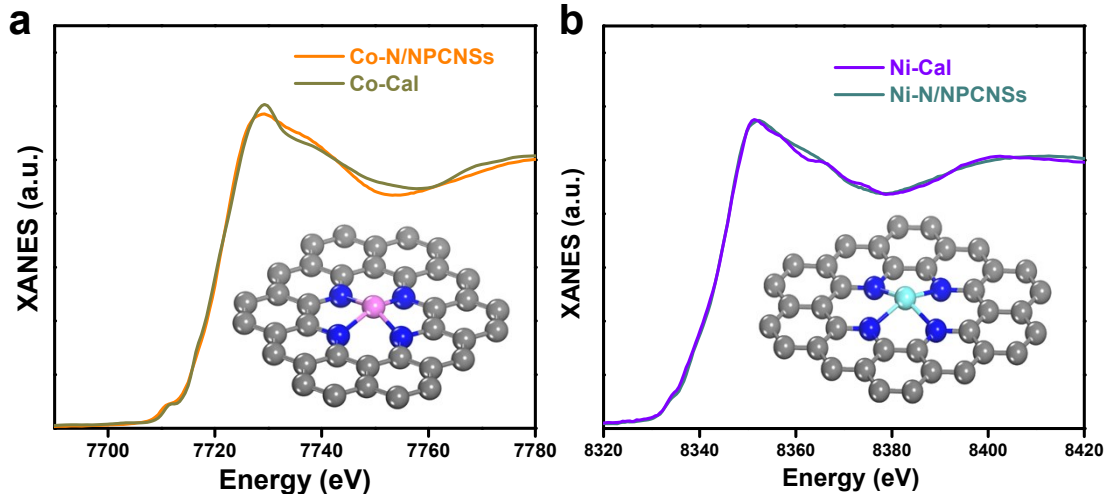

Fig. S15. The simulated XANES spectrum of (a) Co K-edge and (b) Ni K-edge based on Co-N/NPCNSs and Ni-N/NPCNSs, compared with their experimental spectra, respectively.

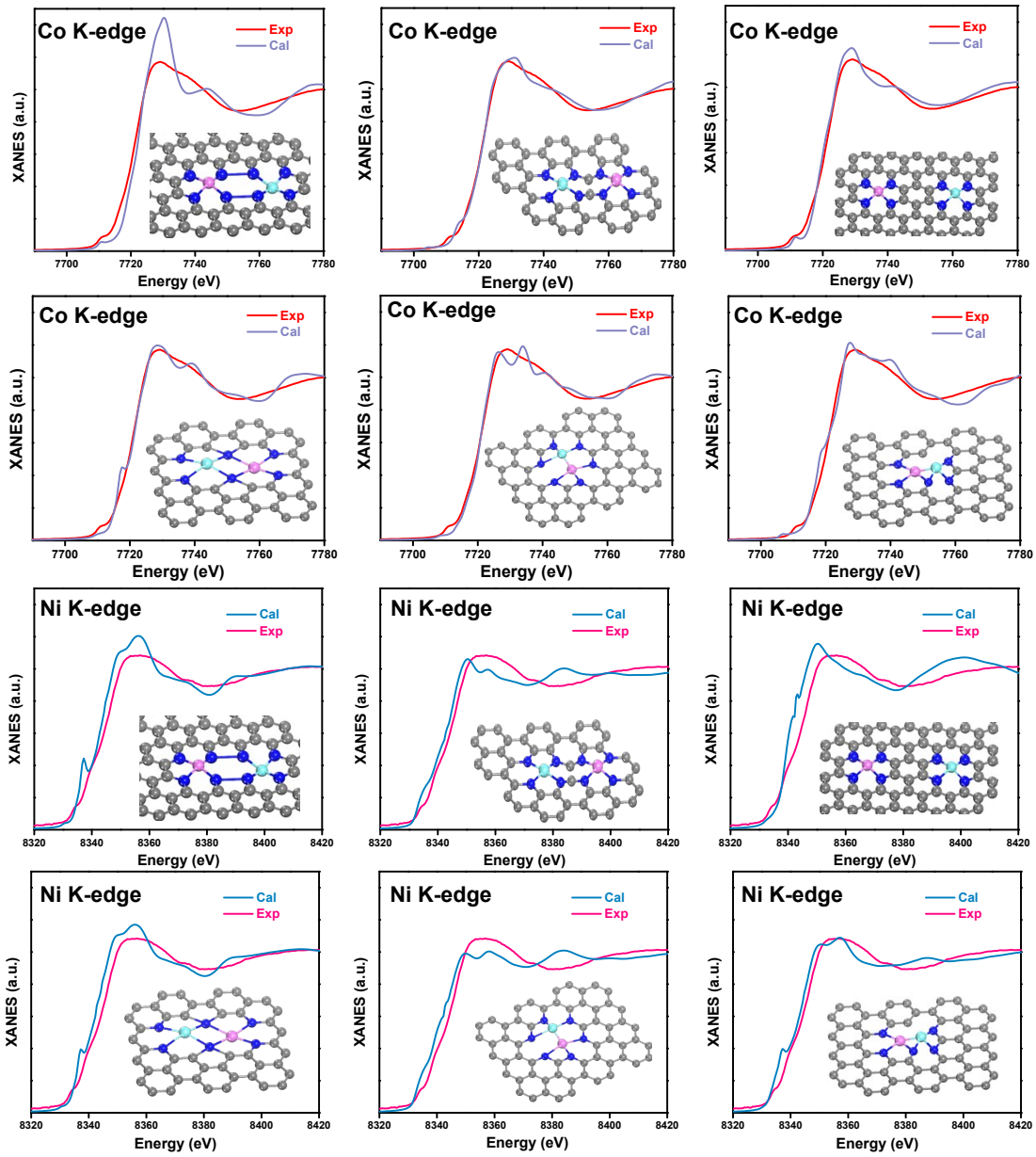

Fig. S16. Comparison between the Co and Ni K-edge XANES experimental spectrum of Co-N-Ni/NPCNSs (red line) and the theoretical spectrum (lilac line) calculated with others different structure models.

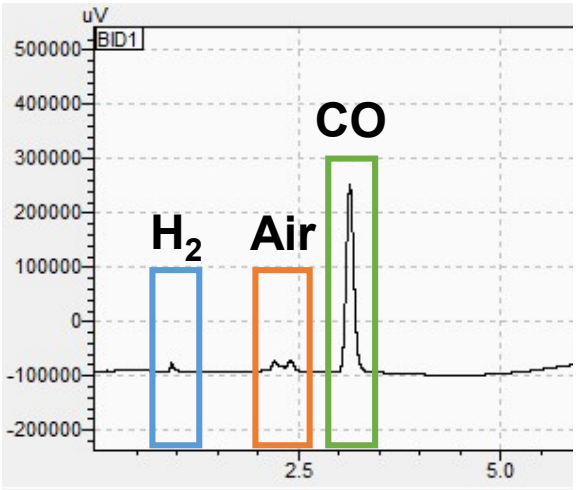

Fig. S17. CO and H_2 were detected by on-line GC at the potential of −0.48 V with respect to Co-N-Ni/NPCNSs catalyst. As shown in the picture, the area of CO product (3.2 min) is far greater than H_2 product (0.9 min), guaranteeing the high performance of Co-N-Ni/NPCNSs catalyst for CO_2RR.

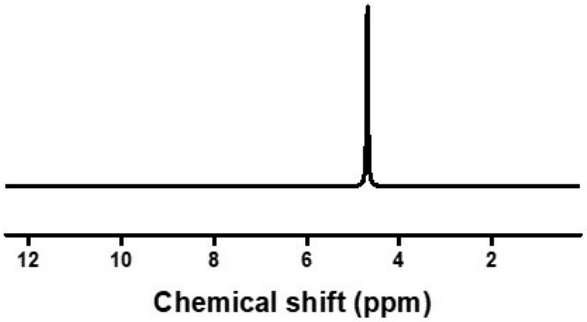

Fig. S18. The ^{1}H NMR spectrum of the electrolyte after CO_2RR electrolysis by using Co-N-Ni/NPCNSs catalyst. It is found that only the water (H_2O) signal appeared, without other signals assigned to liquid products such as formic acid, ethanol, etc.

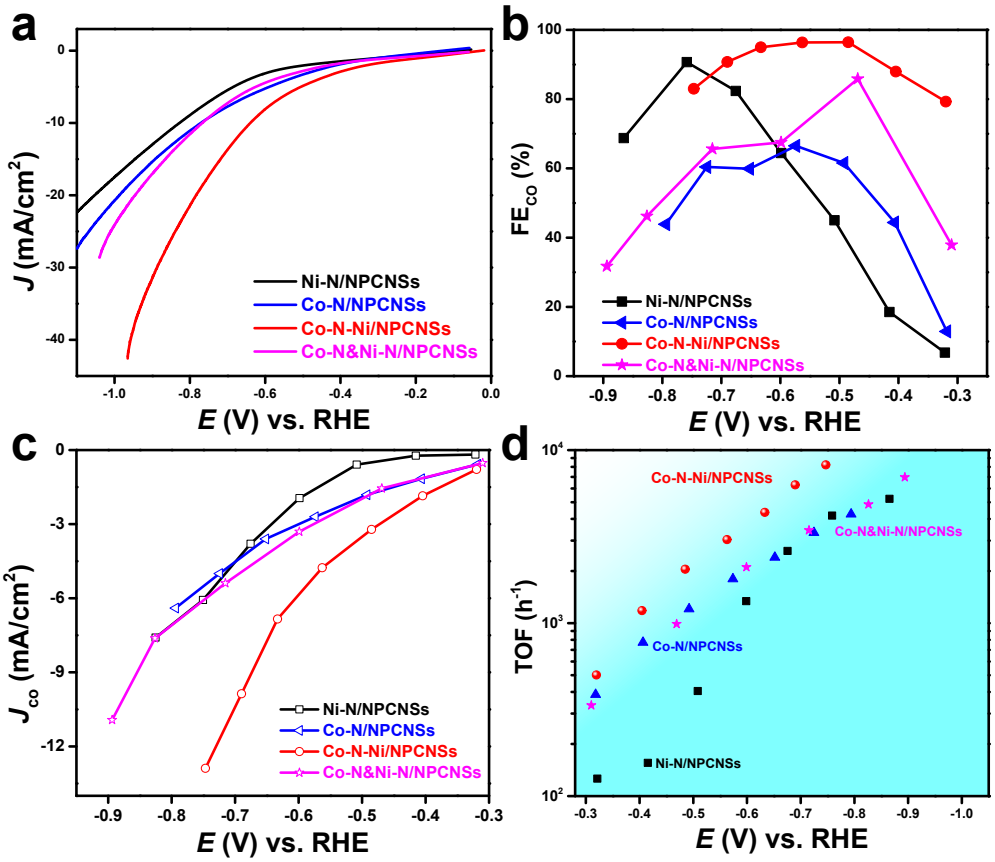

Fig. S19. The CO_2RR performance of Co-N&Ni-N/NPCNSs physical mixture catalyst compared with those of the other three catalysts. a) LSV curves. b) FE_{CO}. c) J_{CO} d) TOF.

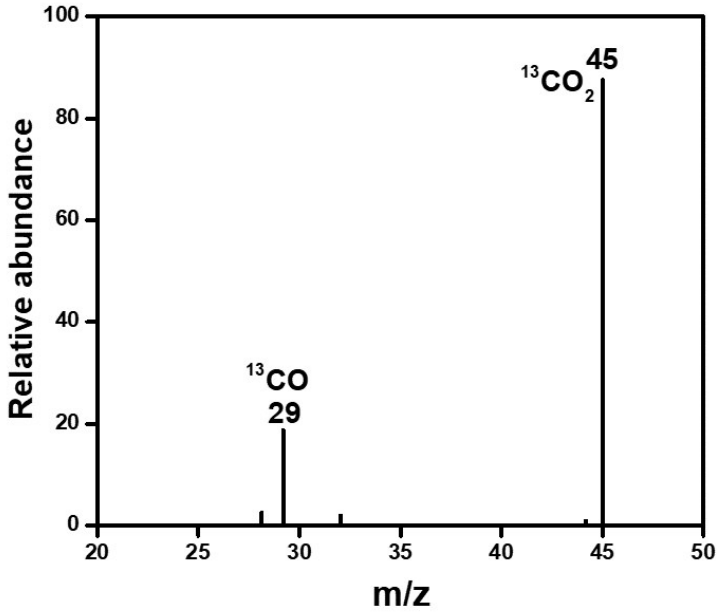

Fig. S20. Mass spectrometry signal of CO_2RR by using $^{13}CO_2$ as the electrocatalytic feedstock. Firstly, $^{13}CO_2$ feedstock was adopted to react with KOH solution to form $^{13}CO_2$-saturated $KH^{13}CO_3$ electrolyte. Then, we continuously pumped $^{13}CO_2$ bubbles into the system and carried out CO_2RR experiment under constant potential. Finally, we collected the gaseous products using a drainage method, followed by mass spectrometry detection. From mass spectrometry (Fig. R24), we clearly observed that the peaks at 29 and 45 positions assigned to ^{13}CO product and $^{13}CO_2$ feedstock, respectively. Of course, the system is not completely air-tight, causing a small amount of air (N_2 at 28 and O_2 at 32 position) to leak into the system.

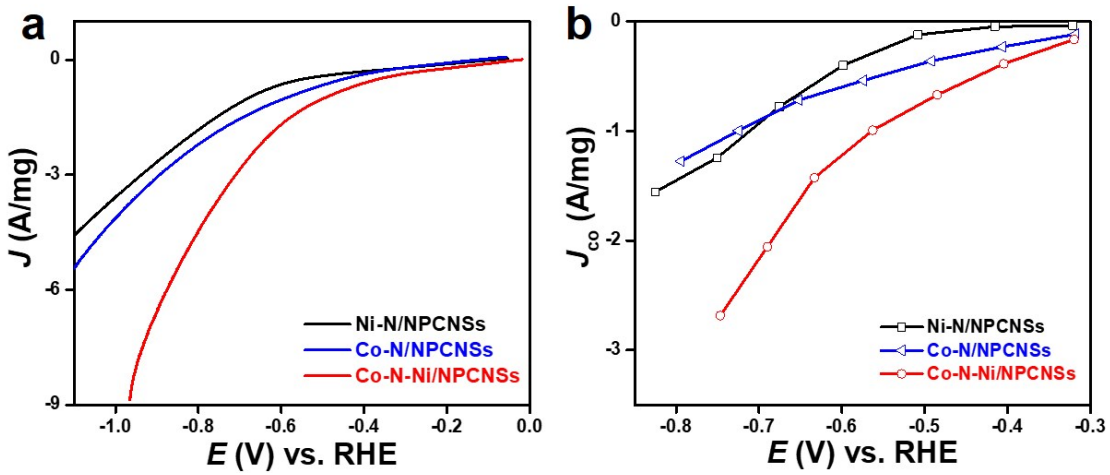

Fig. S21. The normalized mass activity of Co-N-Ni/NPCNSs, Co-N/NPCNSs and Ni-N/NPCNSs catalysts. (a) LSV curves, (b) *J*co.

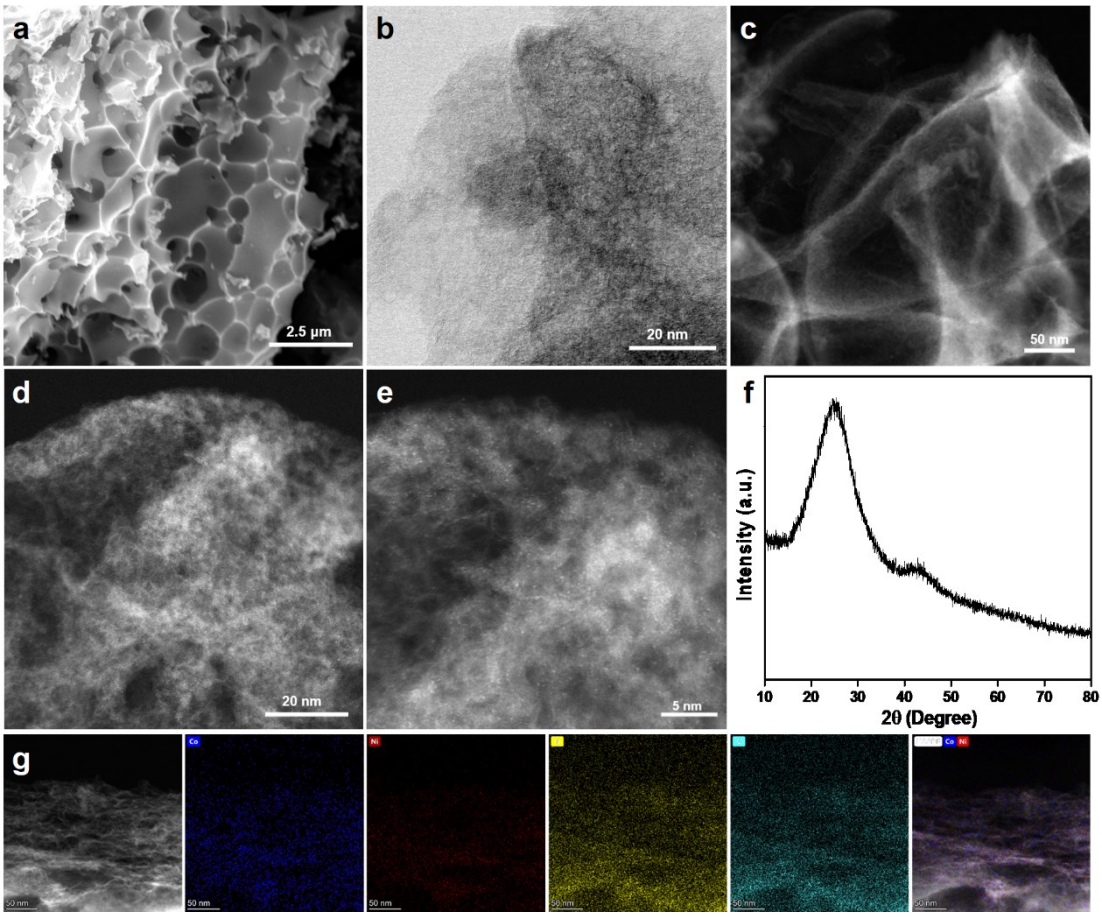

Fig. S22. Morphologies and XRD pattern of Co-N-Ni/NPCNSs catalyst after CO_2RR stability test. a) SEM. b) High-resolution TEM. c) HAADF-STEM. d) AC-STEM. e) The magnified AC-STEM. f) XRD pattern. g) EDS mappings.

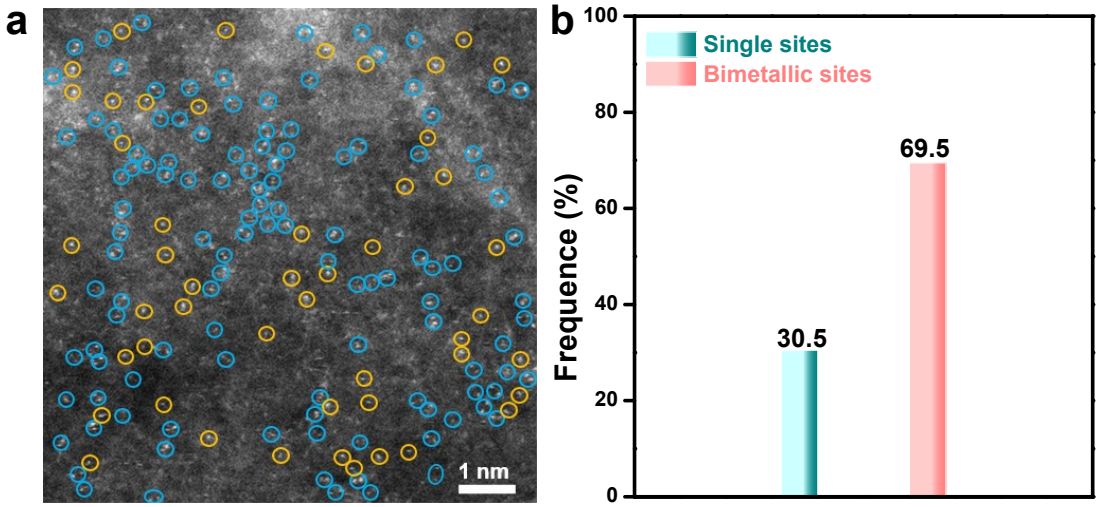

Fig. S23. (a) The AC-STEM image of Co-N-Ni/NPCNSs catalyst after stability testing. The bimetallic sites and single sites were circled with blue and orange circle, respectively. (b) Statistical the density of Co-N-Ni bimetallic sites and single sites in AC-STEM image.

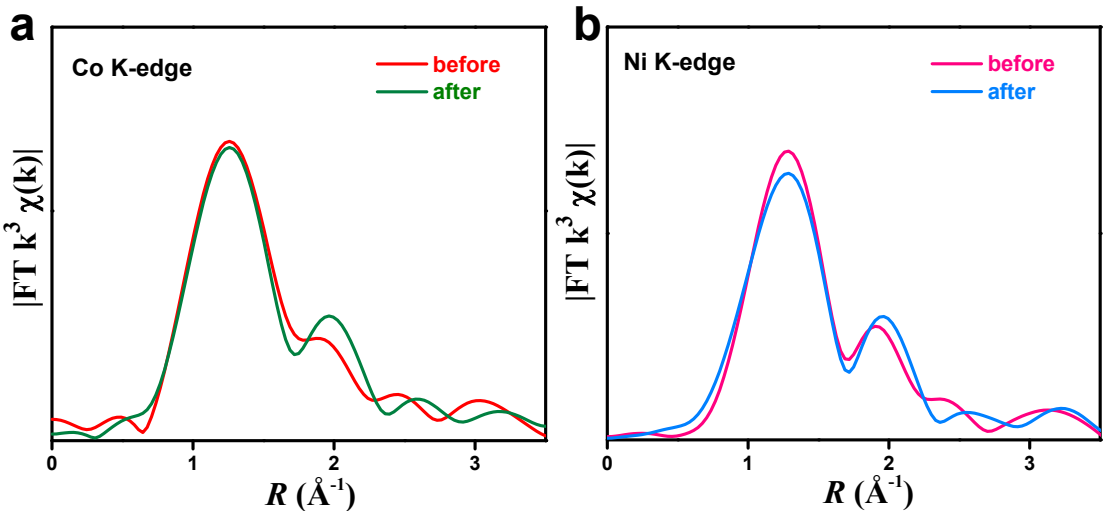

Fig. S24. The Co (a) and Ni (b) K-edge EXAFS spectra of Co-N-Ni/NPCNSs catalyst after stability testing compared to the initial EXAFS spectra, respectively.

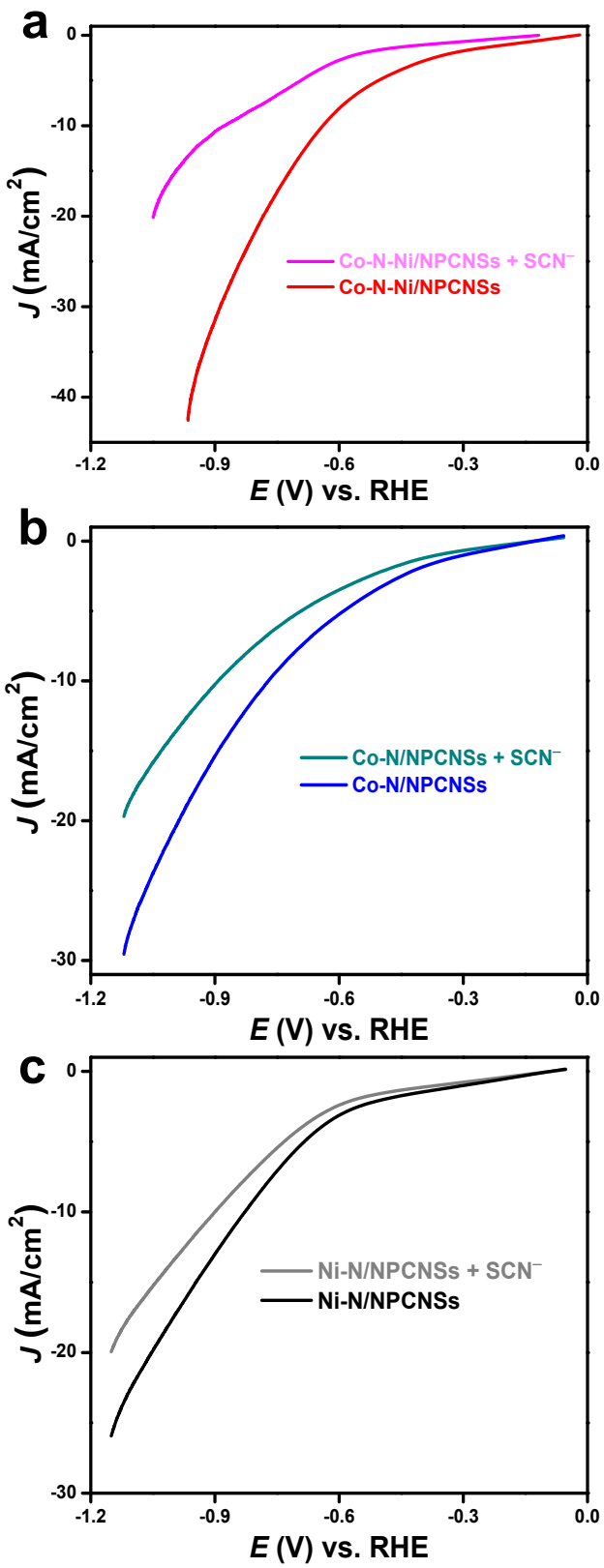

Fig. S25. LSV curves of three catalysts were measured in a CO_2-saturated 0.1M $KHCO_3$ + 0.02 M KSCN solution (a) Co-N-Ni/NPCNSs, (b) Co-N/NPCNSs, (c) Ni-N/NPCNSs.

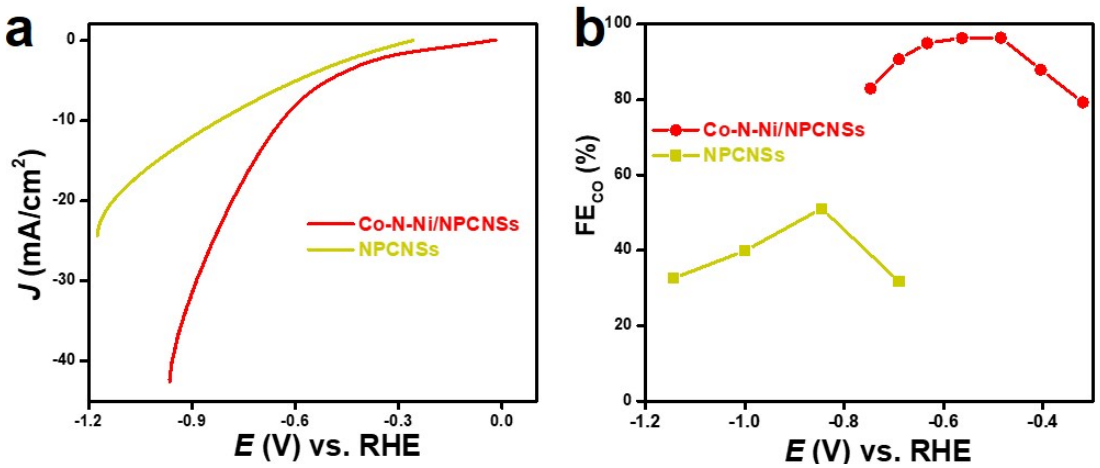

Fig. S26. The CO_2RR performance of Co-N-Ni/NPCNSs and NPCNSs samples. a) LSV curves. b) FE_{CO}.

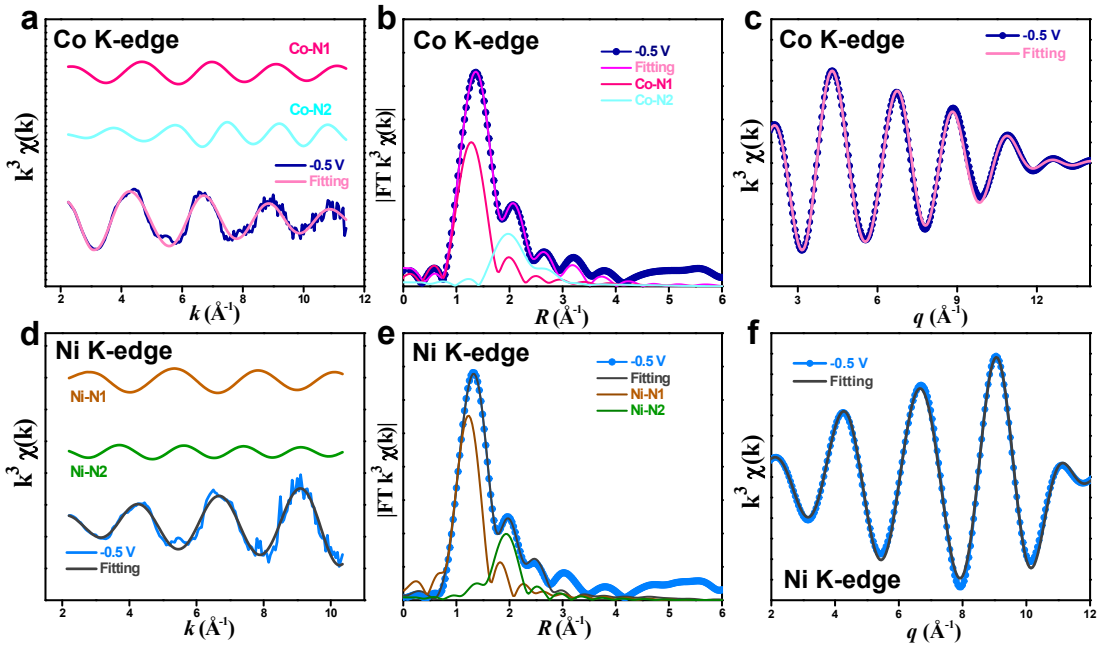

Fig. S27. The in-situ FT-EXAFS fitting curve in light of Co-N-Ni/NPCNSs at an applied voltage of −0.5 V. (a) The *k*-space EXAFS curve at Co K-edge. (b) The *R*-space EXAFS curve at Co K-edge. (c) The *q*-space EXAFS curve at Co K-edge. (d) The *k*-space EXAFS curve at Ni K-edge. (e) The *R*-space EXAFS curve at Ni K-edge. (f) The *q*-space EXAFS curve at Ni K-edge.

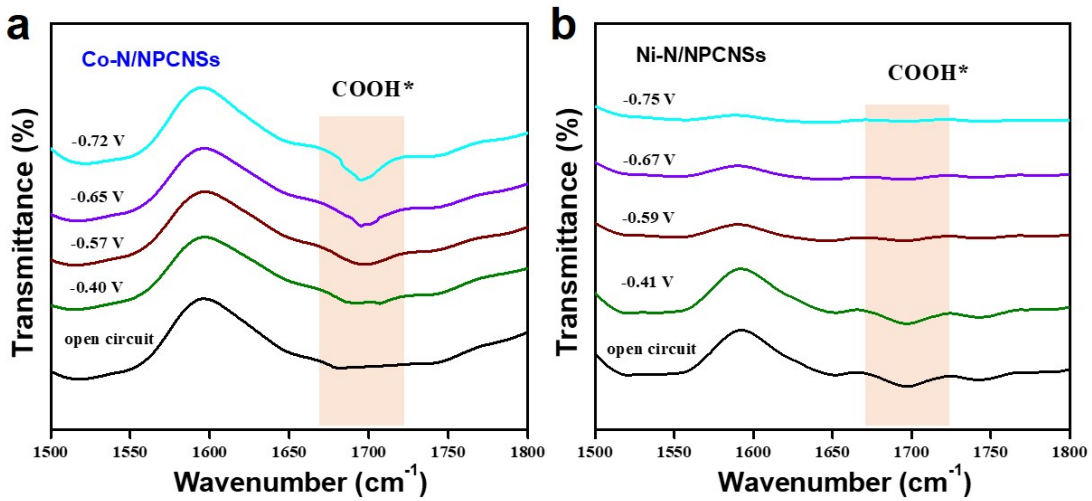

Fig. S28. In situ SR-FTIR spectroscopy measurements of Co-N/NPCNSs (a) and Ni-N/NPCNSs (b).

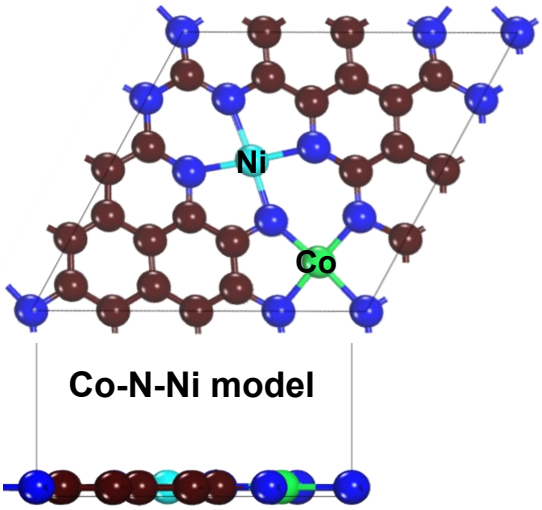

Fig. S29. The schematic model structure of N-bridged Co-N-Ni bimetallic structure in Co-N-Ni/NPCNSs catalyst.

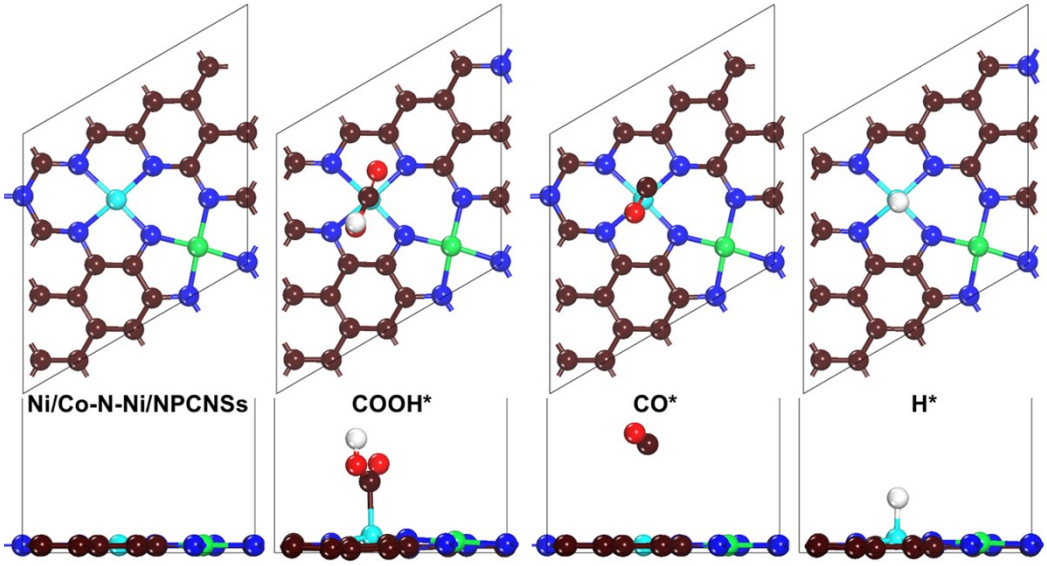

Fig. S30. Model structure and adsorption configurations of COOH, CO and H on the Ni site of the Co-N-Ni bimetallic sites (Ni/Co-N-Ni) (C in black, O in red, N in blue, H in white, Co in green and Ni in cyan).

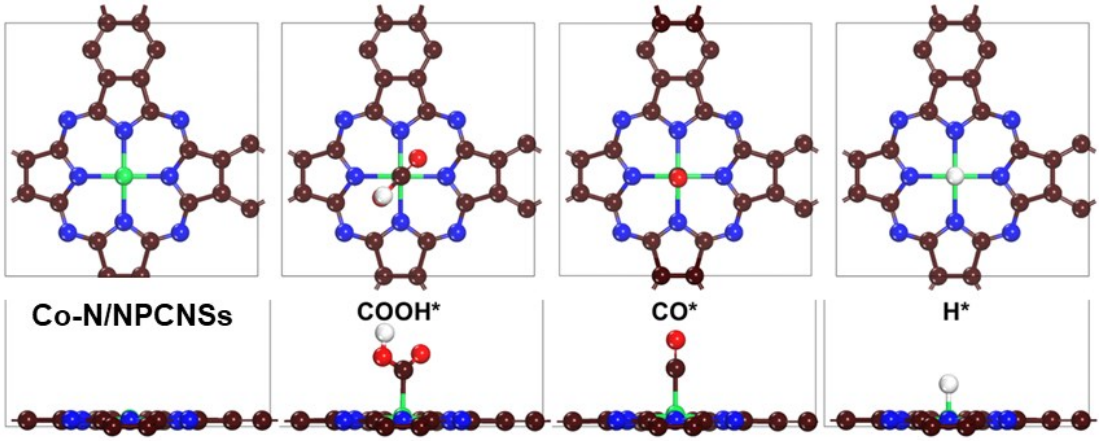

Fig. S31. Model structure and adsorption configurations of COOH, CO and H on Co-N site. (C in black, O in red, N in blue, H in white, and Co in green).

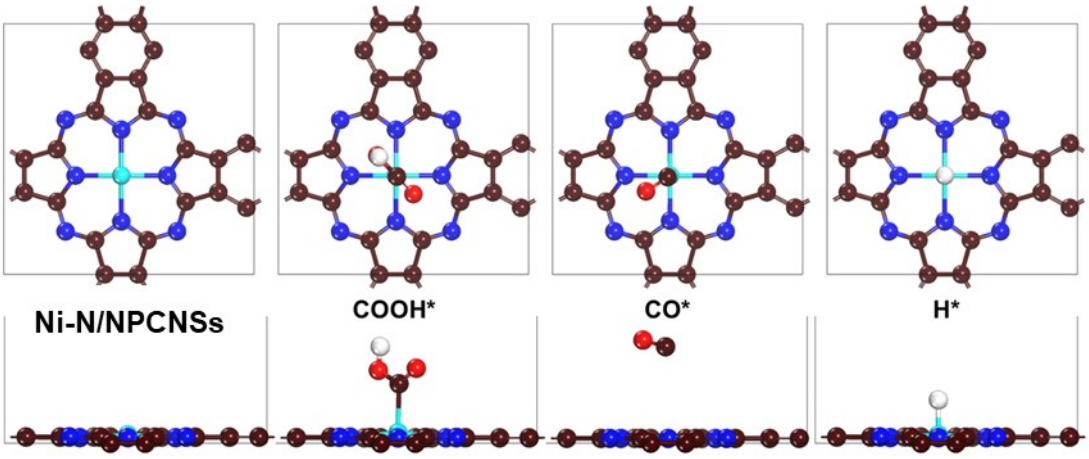

Fig. S32. Model structure and adsorption configurations of COOH, CO and H on Ni-N site. (C in black, O in red, N in blue, H in white, and Ni in cyan).

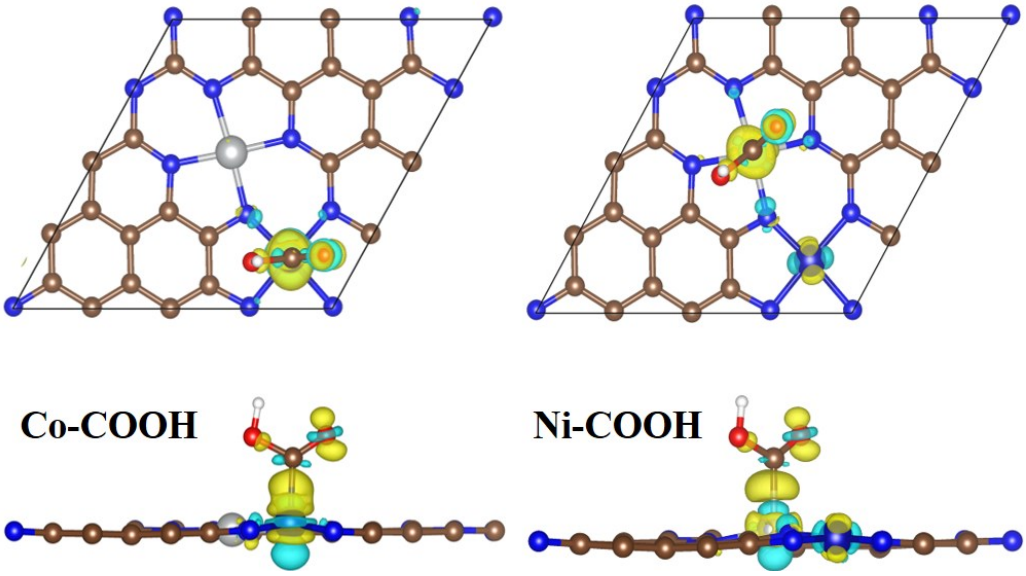

Fig. S33. The charge density difference of COOH* on Co (left) and Ni (right) sites of Co-N-Ni structure, where the isosurface value is set to be 0.05 e $Å^{-3}$ and the charge accumulated and depleted regions are shown in yellow and cyan, respectively.

Table S1. ICP-MS results of the three catalysts.

Sample	Co (wt%)	Ni (wt%)
Co-N-Ni/NPCNSs	0.119	0.121
Co-N/NPCNSs	0.251	/
Ni-N/NPCNSs	/	0.244

Table S2. The each type of N species content of Co-N-Ni/NPCNSs, Co-N/NPCNSs and Ni-N/NPCNSs catalysts.

Sample	Pyridinic N (at%)	Co/Ni-N (at%)	Pyrrolic N (at%)	Graphitic N (at%)
Co-N-Ni/NPCNSs	1.36	0.38	0.82	0.47
Co-N/NPCNSs	0.96	0.28	0.64	0.41
Ni-N/NPCNSs	1.08	0.31	0.60	0.28

Table S3. Structural parameters extracted from the Co K-edge EXAFS fitting. (S_0^2=0.81)

sample	Scattering pair	CN	R(Å)	$\sigma^2(10^{-3}Å^2)$	ΔE_0(eV)	R factor
Co-N-Ni/ NPCNSs	Co-N1	3.2±0.6	1.94±0.01	6.1±0.7	1.5±0.5	0.008
	Co-N2	0.9±0.3	1.97±0.01	5.7±0.5		
Co-N/NPCNSs	Co-N	4.1±0.5	1.96±0.01	5.4±0.6	1.5±0.5	0.006

S_0^2 is the amplitude reduction factor; CN is the coordination number; R is interatomic distance (the bond length between central atoms and surrounding coordination atoms); σ^2 is Debye-Waller factor (a measure of thermal and static disorder in absorber-scatterer distances); ΔE_0 is edge-energy shift (the difference between the zero kinetic energy value of the sample and that of the theoretical model). R factor is used to value the goodness of the fitting.

Error bounds that characterize the structural parameters obtained by EXAFS spectroscopy were estimated as N ± 20%; R ± 1%; σ^2 ± 20%; ΔE_0 ± 20%.

Table S4. Structural parameters extracted from the Ni K-edge EXAFS fitting. (S_0^2=0.76)

sample	Scattering pair	CN	R(Å)	$\sigma^2(10^{-3}Å^2)$	ΔE_0(eV)	R factor
Co-N-Ni/ NPCNSs	Ni-N1	3.1±0.5	1.92±0.01	6.2±0.8	1.5±0.5	0.006
	Ni-N2	1.1±0.3	1.97±0.01	5.1±0.6		
Ni-N/NPCNSs	Ni-N	3.9±0.6	1.95±0.01	5.9±0.6	2.0±0.5	0.007

S_0^2 is the amplitude reduction factor; CN is the coordination number; R is interatomic distance (the bond length between central atoms and surrounding coordination atoms); σ^2 is Debye-Waller factor (a measure of thermal and static disorder in absorber-scatterer distances); ΔE_0 is edge-energy shift (the difference between the zero kinetic energy value of the sample and that of the theoretical model). R factor is used to value the goodness of the fitting.

Error bounds that characterize the structural parameters obtained by EXAFS spectroscopy were estimated as N ± 20%; R ± 1%; σ^2 ± 20%; ΔE_0 ± 20%.

Table S3. Comparison the CO_2RR performance of Co-N-Ni/NPCNSs catalyst at the similar low overpotential with the other reported Co, Fe and Ni based single-atom catalysts.

Catalyst	Overpotential (mV)	FE_{CO} (%)	$-J_{CO}$ ($mA \cdot cm^{-2}$)	TOF (h^{-1})	Ref.
Co-N-Ni /NPCNSs	370	96.4	3.2	2049	**This work**
NapCo@SNG	390	75	~0.23	~79	S10
COF-367-Co	560	91	3.0	1900	S11
CoPc/CNT	350	59	~0.71	6120	S12
Co-MOF	390	56	~1.0	200 (590 mV)	S13
Co-N_2	350	75	~6 (450 mV)	5000	S14
Co-N_4	710	~4.2	/	/	S14
Co_1-N_4	390	30	~0.8	~80	S15
Co-N_5	370	82	~4.5 (620 mV)	480.2 (620 mV)	S16
CoPPc/CNT	375	~84	~4.6	~1200	S17
CoPP@CNT	390	80	~0.74	1224	S18
STPyP-Co	410	~82	/	/	S19
CoFPc	390	<80	/	468	S20
Co-N-C	380	40	~0.4	/	S21
Fe-N-C	380	90	~1.4	/	S21
Fe-N-C	390	90	~0.5	500	S22
Fe^{3+}-N-C	340	94	~16	~1030	S23
H-M-G (FeN_5)	350	97	~1.8	/	S24
Fe-N-C	490	80	/	/	S25
Fe-N-C	490	91	/	/	S26
Fe/NG-750	460	80	~1.7	/	S27
Fe-N-C	360	85	~1.2	/	S28
Co-N-C	440	~20	~1.5	/	S29
Fe-N-C	440	65	~2.1	/	S29
Fe-N/CNF-2	420	95	4.47	3104	S30

Table S3. Continue.

Ni_1-N-C	390	58	~2.9	~300	S31
Ni_{SA}-N_2-C	490	~62	~1.6	~250	S32
Ni_{SA}-N_4-C	490	~38	/	<50	S32
Ni-CNT-CC	350	92	~1	~180	S33
Ni-N_4 SAC	390	54	~7 (590 mV)	~2000	S34
NC-CNTs (Ni)	490	~68	1	~1000	S35
Ni/Fe-N-C	390	90	~0.5	~200	S22
Ni-N-C	390	70	~0.2	~50	S22
SE-Ni SAs@PNC	390	~72	~0.4	611	S36
A-Ni-NSG	410	97	~2.4	~900	S37
Ni-N-C	480	90	~1.4	150	S38
Ni-N-C	715	70	~0.6	544	S29
Ni SAs/N-C	590	55	~2.5	803	S39

Table S6. Structural parameters extracted from the Co and Ni K-edge EXAFS fitting.

Sample	Scattering pair	CN	R(Å)	$\sigma^2(10^{-3}Å^2)$	ΔE_0(eV)	R factor
Co(-0.5 V)	Co-N1	3.1±0.5	1.97±0.01	6.4±0.7	1.5±0.5	0.006
	Co-N2	1.0±0.3	2.00±0.01	5.9±0.7		
	Co-C	1.0±0.3	2.01±0.01	5.9±0.5		
Ni(-0.5 V)	Ni-N1	2.9±0.4	1.96±0.01	6.5±0.7	1.5±0.5	0.007
	Ni-N2	1.2±0.3	2.01±0.01	5.4±0.6		
	Ni-C	1.1±0.3	2.00±0.01	6.1±0.7		

S_0^2 is the amplitude reduction factor; CN is the coordination number; R is interatomic distance (the bond length between central atoms and surrounding coordination atoms); σ^2 is Debye-Waller factor (a measure of thermal and static disorder in absorber-scatterer distances); ΔE_0 is edge-energy shift (the difference between the zero kinetic energy value of the sample and that of the theoretical model). R factor is used to value the goodness of the fitting.

Error bounds that characterize the structural parameters obtained by EXAFS spectroscopy were estimated as N ± 20%; R ± 1%; σ^2 ± 20%; ΔE_0 ± 20%.

References

S1 P. Zhang, P. Fritz, K. Schroen, H. Duan, R. Boom, M. Chan-Park, ACS *Appl. Mater. Interfaces,* 2018, **10**, 33564-33573.

S2 B. Ravel, M. Newville, *Phys. Scr.,* 2005, **T115**, 1007-1010.

S3 G. Kresse, J. Furthmüller, *Comput. Mater. Sci.,* 1996, **6**, 15-50.

S4 G. Kresse, J. Furthmüller, *Phys. Rev. B,* 1996, **54**, 11169-11186.

S5 P. Blöchl, *Phys. Rev. B*, 1994*,* **50**, 17953-17979.

S6 G. Kresse, D. Joubert, *Phys. Rev. B,* 1999, **59**, 1758-1775.

S7 B. Hammer, B. Hansen, J. Nørskov, *Phys. Rev. B,* 1999, **59**, 7413-7421.

S8 J. Nørskov, J. Rossmeisl, A. Logadottir, L. Lindqvist, J. Kitchin, T. Bligaard, H. Jónsson, *J. Phys. Chem. B,* 2004, **108**, 17886-17892.

S9 A. Peterson, F. Abild-Pedersen, F. Studt, J. Rossmeisl, J. Nørskov, *Energy Environ. Sci.,* 2010, **3**, 1311-1315.

S10 J. Wang, X. Huang, S. Xi, J.-M. Lee, C. Wang, Y. Du and X. Wang, *Angew. Chem. Int. Ed.,* 2019, **58**, 13532-13539.

S11 S. Lin, C. Diercks, Y.-B. Zhang, N. Kornienko, E. Nichols, Y. Zhao, A. Paris, D. Kim, P. Yang, O. Yaghi and C. Chang *Science*, 2015, **349**, 1208-1213.

S12 X. Zhang, Z. Wu, X. Zhang, L. Li, Y. Li, H. Xu, X. Li, X. Yu, Z. Zhan, Y. Liang and H. Wang, *Nat. Commun.* 2017, **8**, 14675.

S13 N. Kornienko, Y. Zhao, C. Kley, C. Zhu, D. Kim, S. Lin, C. Chang, O. M. Yaghi and P. Yang, *J. Am. Chem. Soc.,* 2015, **137**, 14129-14135.

S14 X. Wang, Z. Chen, X. Zhao, T. Yao, W. Chen, R. You, C. Zhao, G. Wu, J. Wang, W. Huang, J. Yang, X. Hong, S. Wei, Y. Wu and Y. Li, *Angew. Chem. Int. Ed.,* 2018, **57**, 1944-1948.

S15 Z. Geng, Y. Cao, W. Chen, X. Kong, Y. Liu, T. Yao and Y. Lin, *Appl. Catal. B-Environ.,* 2019, **240**, 234-240.

S16 N. Han, Y. Wang, L. Ma, J. Wen, J. Li, H. Zheng, K. Nie, X. Wang, F. Zhao,1 Y. Li, J. Fan, J. Zhong, T. Wu, D. Miller, J. Lu, S.-T. Lee and Y. Li, *Chem,* 2017, **3**, 652-664.

S17 Y. Pan, R. Lin, Y. Chen, S. Liu, W. Zhu, X. Cao, W. Chen, K. Wu, W-C. Cheong, Y. Wang, L. Zheng, J. Luo, Y. Lin, Y. Liu, C. Liu, J. Li, Q. Lu, X. Chen, D. Wang, Q. Peng, C. Chen and Y. Li, *J. Am. Chem. Soc.,* 2018, **140**, 4218-4221.

S18 M. Zhu, J. Chen, L. Huang, R. Ye, J. Xu and Y.-F. Han, *Angew. Chem. Int. Ed.,* 2019, **58**, 6595-6599.

S19 J. Han, P. An, S. Liu, X. Zhang, D. Wang, Y. Yuan, J. Guo, X. Qiu, K. Hou, L. Shi, Y. Zhang, S. Zhao, C. Long and Z. Tang, *Angew. Chem. Int. Ed.,* 2019, **58**, 12711-12716.

S20 N. Morlanés, K. Takanabe and V. Rodionov, *ACS Catal.,* 2016, **6**, 3092-3095.

S21 F. Pan, H. Zhang, K. Liu, D. Cullen, K. More, M. Wang, Z. Feng, G. Wang, G. Wu and Y. Li, *ACS Catal.,* 2018, **8**, 3116-3122.

S22 W. Ren, X. Tan, W. Yang, S. Xu, K. Wang, S. Smith and C. Zhao, *Angew. Chem. Int. Ed.,* 2019, **58**, 6972-6976.

S23 J. Gu, C.-S. Hsu, L. Bai, H. Chen and X. Hu, *Science,* 2019, **364**, 1091-1094.

S24 H. Zhang, J. Li, S. Xi, Y. Du, X. Hai, J. Wang, H. Xu, G. Wu, J. Zhang, J. Lu and J. Wang, *Angew. Chem. Int. Ed.,* 2019, **58**, 14871-14876.

S25 A. Varela, N. Sahraie, J. Steinberg, W. Ju, H.-S. Oh and P. Strasser, *Angew. Chem. Int. Ed.,* 2015, **54**, 10758-10762.

S26 T. Huan, N. Ranjbar, G. Rousse, M. Sougrati, A. Zitolo, V. Mougel, F. Jaouen and M. Fontecave, *ACS Catal.,* 2017, **7**, 1520-1525.

S27 C. Zhang, S. Yang, J. Wu, M. Liu, S. Yazdi, M. Ren, J. Sha, J. Zhong, K. Nie, A. Jalilov, Z. Li, H. Li, B. I. Yakobson, Q. Wu, E. Ringe, H. Xu, P. Ajayan, J. Tour, *Adv. Energy Mater.,* 2018, **8**, 1703487.

S28 X.-M. Hu, H. Hval, E. Bjerglund, K. Dalgaard, M. Madsen, M.-M. Pohl, E. Welter, P. Lamagni, K. Buhl, M. Bremholm, M. Beller, S. Pedersen, T. Skrydstrup and K. Daasbjerg, *ACS Catal.,* 2018, **8**, 6255-6264.

S29 W. Ju, A. Bagger, G.-P. Hao, A. Varela, I. Sinev, V. Bon, B. Cuenya, S. Kaskel, J. Rossmeisl and P. Strasser, *Nat. Commun.,* 2017, **8**, 944.

S30 Q. Cheng, K. Mao, L. Ma, L. Yang, L. Zou, Z. Zou, Z. Hu and H. Yang, *ACS Energy Lett.,* 2018, **3**, 1205-1211.

S31 L. Jiao, W. Yang, G. Wan, R. Zhang, X. Zheng, H. Zhou, S.-H. Yu and H.-L. Jiang, *Angew. Chem. Int. Ed.,* 2020, **59**, 20589-20595.

S32 Y.-N. Gong, L. Jiao, Y. Qian, C.-Y. Pan, L. Zheng, X. Cai, B. Liu, S.-H. Yu and H.-L. Jiang, *Angew. Chem. Int. Ed.,* 2020, **59**, 2705-2709.

S33 S. Liu, S.-F. Hung, J. Ding, W. Cai, L. Liu, G. Jiajian, l. Xuning, X. Ren, Z. Kuang, Y. Huang, T. Zhang and B. Liu, *Angew. Chem. Int. Ed.,* 2019, **59**, 798-803.

S34 X. Rong, H.-J. Wang, X.-L. Lu, R. Si and T.-B. Lu, *Angew. Chem. Int. Ed.,* 2019,

59, 1961-1965.

S35 Q. Fan, P. Hou, C. Choi, W. Tai-Sing, S. Hong, F. Li, Y.-L. Soo, P. Kang, Y. Jung and Z. Sun, *Adv. Energy Mater.,* 2019, **10**, 1903068.

S36 J. Yang, Z. Qiu, C. Zhao, W. Wei, W. Chen, Z. Li, Y. Qu, J. Dong, J. Luo, Z. Li and Y. Wu, *Angew. Chem. Int. Ed.,* 2018, **57**, 14095-14100.

S37 H. B. Yang, S.-F. Hung, S. Liu, K. Yuan, S. Miao, L. Zhang, X. Huang, H.-Y. Wang, W. Cai, R. Chen, J. Gao, X. Yang, W. Chen, Y. Huang, H. M. Chen, C. M. Li, T. Zhang and B. Liu, *Nat. Energy*, 2018, **3**, 140-147.

S38 F. Pan, W. Deng, C. Justiniano and Y. Li, *Appl. Catal. B-Environ.,* 2018, **226**, 463-472.

S39 C. Zhao, X. Dai, T. Yao, W. Chen, X. Wang, J. Wang, J. Yang, S. Wei, Y. Wu and Y. Li, *J. Am. Chem. Soc.,* 2017, **139**, 8078-8081.